Journal Pre-proof

Exhumation and structural evolution of the high-elevation Malcante Range, Eastern Cordillera, NW Argentina

Patricio Payrola, Sebastian Zapata, Edward R. Sobel, Cecilia del Papa, Heiko Pingel, Johannes Glodny, Jonathan Ledesma

PII: S0895-9811(20)30533-2

DOI: https://doi.org/10.1016/j.jsames.2020.102990

Reference: SAMES 102990

To appear in: *Journal of South American Earth Sciences*

Received Date: 15 June 2020

Revised Date: 22 October 2020

Accepted Date: 24 October 2020

Please cite this article as: Payrola, P., Zapata, S., Sobel, E.R., Papa, C.d., Pingel, H., Glodny, J., Ledesma, J., Exhumation and structural evolution of the high-elevation Malcante Range, Eastern Cordillera, NW Argentina, *Journal of South American Earth Sciences* (2020), doi: https://doi.org/10.1016/j.jsames.2020.102990.

Payrola, P. Conceptualization, Investigation, Formal analysis, Writing - Review & Editing

Zapata, S. Conceptualization, Methodology, Investigation, Writing - Review & Editing

Sobel, E. Conceptualization, Methodology, Investigation, Project administration, Supervision, Writing - Review & Editing, Resources

del Papa, C. Conceptualization, Investigation, Project administration, Supervision, Writing - Review & Editing

Pingel, H. Conceptualization, Investigation, Writing - Review & Editing

Glodney, J. Investigation, Methodology, Writing - Resources

Ledezma, J. Writing

Exhumation and structural evolution of the high-elevation Malcante Range, Eastern Cordillera, NW Argentina

Patricio Payrola[1,a], Sebastian Zapata[4,5], Edward R. Sobel[3], Cecilia del Papa[2], Heiko Pingel[3], Johannes Glodny[6], Jonathan Ledesma[2]

[1]Instituto de Bio y Geociencias del NOA (IBIGEO), CONICET-Universidad Nacional de Salta, Av. Bolivia 5150, 4400 Salta, Argentina.

[2]CICTERRA-F.C.E.FyN. CONICET-Universidad Nacional de Córdoba, Av. Vélez Sarsfield 1611, X5016GCA, Córdoba, Argentina.

[3]Institut für Geowissenschaften, Universität Potsdam, Karl-Liebknecht-Str. 24-25, 14476 Potsdam, Germany.

[4]Smithsonian Tropical Research Institute, PO Box 0843-03092, Balboa, Ancon, Panama.

[5]Department of Geosciences and Geological and Petroleum Engineering, Missouri University of Science and Technology, USA.

[6]Helmholtz-Zentrum Potsdam, Deutsches GeoForschungsZentrum GFZ, Telegrafenberg, 14473 Potsdam, Germany

---

[a]**Corresponding author**.

Patricio Payrola (ppayrola@gmail.com)

Abstract

As an integral part of the Eastern Cordillera, the fault-bounded Malcante mountain range (up to 5,100 m) in the NW Argentine Andes (ca. 25°S) is located in the transition between the arid Puna Plateau to the west and the humid broken foreland to the east. At this latitude, the topographic gradient of the eastern Andean margin forms an efficient orographic barrier that causes pronounced east–west rainfall and surface-process gradients. In this setting, the Malcante Range is an important, yet poorly studied structural high formed during the Cenozoic topographic growth of the Central Andes. In this study, we combine (a) detailed field observations, (b) a two-dimensional structural reconstruction, (c) apatite fission track and (U-Th-Sm)/He thermochronology of bedrock samples from a vertical transect across the western flank of the Malcante Range, and (d) inverse thermal modelling using QTQt software with the aim of deciphering the exhumation history of this mountain range. Field data indicate the presence of an angular unconformity between Cenozoic foreland deposits and older sedimentary strata, suggesting an initial episode of deformation during the middle-late Eocene, while our thermal model constrains the onset of exhumation at ~10 Ma. We suggest that exhumation was related to the unroofing of the easily erodible sedimentary cover, which prevented significant initial surface uplift. This may have changed as more resilient bedrock was exposed at ~5 Ma according to the thermal model, promoting rapid rock uplift. In combination with published data, our thermochronology allows us to speculate on the existence of a zone of deformation concentrated in the area of the present-day Pasha (24.5°S), Malcante (25°S), and Agua de Castilla (25.4°S) mountain ranges by ca. 10 Ma.

Keywords

Thermochronology, apatite fission track, apatite (U–Th)/He, mountain building, Eastern Cordillera, NW Argentina

1. Introduction

The orogenic wedge model predicts that a pulse of rock uplift causes an instantaneous erosional response, and explains the conditions in which deformation propogates in a forward sequence at the orogen scale (e.g., Davis et al., 1983; Dahlen, 1990). In a contractile setting, significant fault displacement can strongly influence the distribution of rainfall, erosion, and vegetation cover (Lenters and Cook, 1997; Bookhagen and Strecker, 2012; Burbank et al., 2012; Pingel et al., 2020). In basement-involved provinces, deformation is accomodated by a combination of reactivation of pre-existing heterogeneities and the generation of new faults (Burtman, 1975; Sibson, 1995; Holdsworth et al., 2001; Buiter and Pfiffner, 2003).

The Cenozoic topographic growth of the Central Andes is linked to the eastward propagation of deformation, which is a consequence of the subduction of the oceanic Nazca plate beneath the South American plate (e.g., Barazangi and Isacks, 1976; Jordan et al., 1983). The Andes in NW Argentina at ca. 25°S latitude have been divided into 3 major, roughly N-S-oriented morphotectonic provinces (Fig. 1A). From west to east these are the Puna (high elevation, low relief, arid climate), the Eastern Cordillera (high elevation, high relief, semi-arid climate), and the Santa Bárbara System-broken foreland (distributed range uplifts, humid climate) (Turner, 1979; Allmendinger et al., 1983; Kley and Monaldi, 2002;). The Eastern Cordillera forms an efficient orographic barrier for humid air masses from the Atlantic and the Amazon, which causes strong across-strike climatic and vegetational gradients with high rainfall amounts and dense vegetation (Yungas, Fig. 1B) along its eastern flanks and semi-arid to arid conditions in the Andean hinterland that is also reflected in the generally decreasing surface process rates from east to west (Fig. 1A).

The orogen-scale propagation of Cenozoic deformation formed new faults and caused the reactivation of previously-formed structures between the Puna and the Santa Bárbara System (e.g., Allmendinger et al., 1983, Hongn et al., 2007; Carrapa and DeCelles, 2008; Payrola et al., 2012; Pearson et al., 2013; Reiners et al., 2015). Numerous studies have focused on whether this deformation has propagated in- or out-of-sequence (e.g., Pearson et al., 2013; Zhou et al., 2017; Payrola et al., 2020), and to what extent fault reactivation is promoted by basement heterogeneities (Hongn et al., 2010; Pearson et al., 2013; Payrola et al., 2020; Zapata et al., 2020). The main precursors of out-of-sequence deformation are: 1) fault-properties (e.g., fault orientation, fluid pressure, friction coefficient); 2) shortening rate; 3) lithology and rock rheology; and 4) the state of lithostatic stress caused by tectonic loading or erosional unloading (e.g., Beaumont et al., 1992;

Willett, 1999; Hilley et al., 2005; Pingel et al., 2013; Ballato et al., 2019). As this deformation propagates eastward, the growth of mountain ranges formed orographic barriers that focussed erosion and caused a W-E gradient in rainfall (e.g., Pingel et al., 2014; Pingel et al., 2019).

Since the Paleogene, deformation in the present-day Eastern Cordillera and parts of the eastern Puna Plateau has been localized by the reactivation of Cretaceous rift NNW-SSE-trending structures that root in the Neoproterozoic-Lower Cambrian basement (Fig. 1A). Under a compressional stress regime, reactivation of Cretaceous normal faults with a thin sedimentary cover (<5,000 m) leads to high-angle basement reverse faults, and hence, thick-skinned deformation (Grier et al., 1991; Hongn and Seggiaro, 2001; Carrera and Muñoz, 2013). The first documented compressional event occurred in the middle-late Eocene, marked by local angular unconformities, growth-strata, deposition of coarsening upward alluvial successions, and AHe and AFT cooling ages along the Puna-Eastern Cordillera margin (Hongn et al 2007; Payrola et al 2009; Pearson et al., 2012). Oligocene to early Miocene compressional events are well-documented in the Puna-Eastern Cordillera margin as well as in the interior of the Eastern Cordillera by local unconformities, growth-strata, seismites, and AFT ages (e.g., Deeken et al., 2006; Payrola et al., 2020; Espinoza et al., 2020). Middle-late Miocene to Pliocene compressional events created high topography in the interior of the Eastern Cordillera according to structural and cooling ages data (Carrera and Muñoz, 2008; Hain et al., 2011; Carrapa et al., 2011; Pearson et al., 2013). Finally, Quaternary compressional events modified the landscape and produced large alluvial fan conglomerates (Bookhagen and Strecker, 2012; McCarthy et al., 2019). However, the ages, rates and mechanisms of particularly each range uplift that led to the present-day topography in the area remain unresolved.

The topography of the Eastern Cordillera shows two main steps (Figs. 1A and C): from 1,200 m mean elevation in the eastern Lerma Valley, including 4,200 m peaks, to 2,500 m mean elevation in the western Calchaquí region, including 5,100 m peaks and minors ranges of 3,000 m in intermediate zones. This topography is partially controlled by reverse fault displacements and by a W-E gradient in rainfall and erosion (Bookhagen and Strecker, 2012; Pingel et al., 2020).

The Calchaqui region, located in the Eastern Cordillera morphotectonic province, comprises several high-elevation ranges in excess of 5,000-6,000 m (e.g., Cachi 6,300, Luracatao 5,900, Acay

5,700, San Miguel 5,700 m, Tirao 5,000, Malcante 5,200, high mountains, Figs. 1A and C). These ranges are integrated by a pre-Cenozoic basement composed by igneous (Luracatao), medium grade metamorphic (Cachi) or very low grade metamorphic rocks (to the east of Cachi Range), and are generally bounded by basement-involved, high-angle reverse faults with kilometric-scale displacements that show a complex deformation history (Hongn and Seggiaro, 2001; Pearson et al., 2012; Payrola et al., 2020). Moreover, lower mountain ranges could have absorbed less shortening than higher mountains at the latitudinal regional scale during the Cenozoic multi-episode of fault-reactivation (e.g., Pearson et al., 2013; Payrola et al., 2020). A particularly interesting topographic feature is the more than 5,000-m high Malcante Range, located on the eastern border of the semi-arid Calchaquí region at ca. 25°S (Figs. 1A and 2). The Malcante Range forms the orographic barrier that limits the heavily vegetated Yungas belt (Fig. 1B), where strong convective storms discharge heavy rains (Hongn and Seggiaro, 2001; Salfity, 2004; Bookhagen and Strecker, 2012). This range also separates the Calchaquí Cenozoic Basin to the west, from the Lerma Valley Basin to the east (Fig. 2); the latter is located in the broken foreland of NW Argentina (Hain et al., 2011; Pearson et al., 2013).

In this study, we analyze the structural geometry of the Cenozoic Malcante Range to understand the details of its formation. To achieve this, we developed a 2D kinematic structural model based on field observations and evaluate the exhumation history using low-temperature apatite (U-Th-Sm)/He and fission track thermochronology. Moreover, we use inverse thermal modelling to recognize rapid cooling episodes and interpret the timing of exhumation of the Malcante Range and compare it with the history of other ranges in the Central Andes. The results improve our understanding of the Miocene orogenic growth, which represents the main phase of deformation in the Central Andes (Jordan et al., 1983; Grier et al., 1991; Coutand et al., 2001; among others).

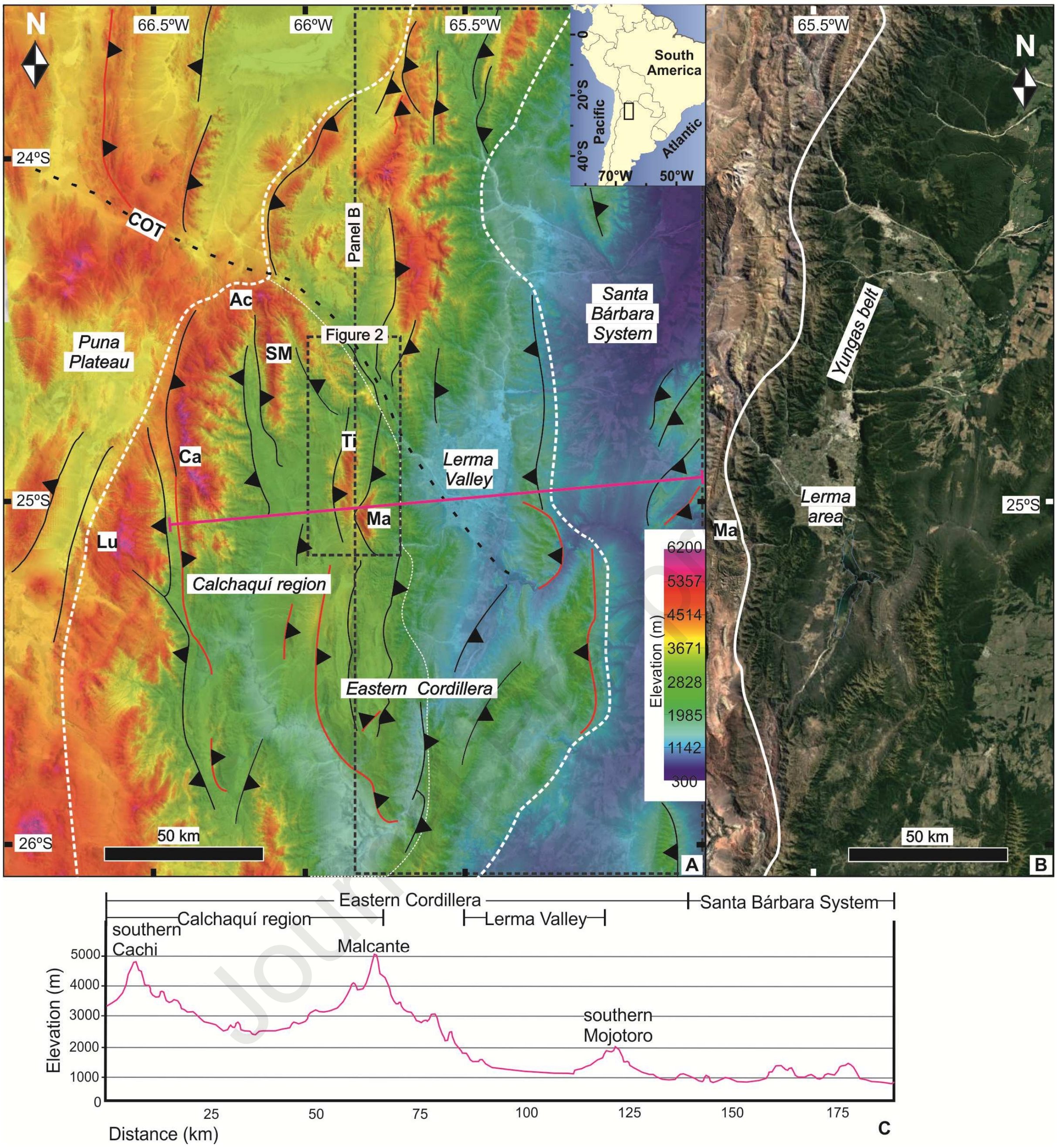

Fig. 1. A. Digital elevation map (JAXA/METI 2010) highlighting regional faults. Cenozoic reverse faults are shown by black lines and Cretaceous inverted faults are shown by red lines (based on Hongn and Seggiaro, 2001; Salfity and Monaldi, 2006). Thick dashed white lines outline morphotectonic units (after Ramos, 1999) and thick dashed black line outlines the Calama-El Toro Lineament (COT). Specific high mountains within the Calchaquí Region: Ca-Cachi, Lu-Luracatao, Ac-Acay, SM-San Miguel, Ti-Tirao, Ma-Malcante. Inset shows location of the study area within South America. **B.** Google Earth image of the eastern border of the Calchaquí region, shown by white solid line, and the heavily vegetated Yungas green belt. Note that the generally lighter tones west of the Calchaquí border reflect less vegetation due to more arid conditions; darker tones farther east reflect much more abundant vegetation linked to higher mean annual precipitation.

2. Geological setting

The Calchaquí region is located in the southernmost part of the Eastern Cordillera at 65.7ºW longitude, between 24.5ºS and 26.5ºS latitudes (Fig. 1). Here, a complex geological history is documented by Neoproterozoic-to-Lower-Cambrian basement rocks and a sedimentary cover recording Cretaceous rifting and Cenozoic foreland deposits (Fig. 2A, Hongn and Seggiaro, 2001). The Calchaquí region constitutes a series of approximately north-south oriented intermontane basins and intervening ranges related to regional faults and folds with the same strike (Salfity, 2004; Salfity and Monaldi, 2006). The regional structural style is characterized by a thick-skinned fold-and-thrust belt formed by mostly west-vergent and subordinate east-vergent faults, and the Cenozoic inversion of NW-SE-oriented Cretaceous normal faults (Hongn and Seggiaro, 2001, Carrera and Muñoz, 2013). Many of the major folds comprise basement-cored ranges with a passively-folded sedimentary cover (i.e., drape folds, e.g., Carrera et al., 2009; Payrola et al., 2012, Hernández et al., 2016).

The regional Neoproterozoic-Lower Cambrian basement is mainly composed of low-grade metamorphic rocks of the Puncoviscana Formation (Turner, 1960; Escayola et al., 2011; Do Campo et al., 2013) with granitic intrusions in the western zone of the Cachi Range (Hongn and Seggiaro, 2001). These rocks are pervasively folded in various wavelengths ranging between 10^{-2} and 10^{2} m, with a predominantly N-S-oriented axial direction concordant with the main foliations and the orientation of ductile shear zones in the region (Hongn and Seggiaro, 2001; Riller and Hongn, 2003; Hernández et al., 2016).

The basement is overlain by the Cretaceous to Paleogene Salta Group (Turner, 1959), which has been subdivided into the syn-rift Pirgua Subgroup and post-rift Balbuena and Santa Bárbara subgroups (Fig. 2A, reviewed in Marquillas et al., 2005). The synrift deposits consist of conglomerate, sandstone, and mudstone deposited in proximal to distal positions of alluvial fans to fluvial systems with volcanic intrusions in the lower and middle sections (Marquillas et al., 2005). Post-rift sediments are characterized by lacustrine to shallow marine carbonates of the Yacoraite Formation and mainly sandstones of fluvial origin (Marquillas et al., 2005).

These units are unconformably overlain by the up to 6,000-m thick Payogastilla Group (Díaz and Malizzia, 1983; Jordan and Alonso, 1987; Hongn et al., 2007), composed of an Eocene to Pleistocene assemblage of fluvial, alluvial, and eolian deposits (Fig. 2A), which document the transition from unconstrained foreland deposition to the present-day restricted intermontane basin deposition (Díaz and Malizzia, 1983; Coutand et al., 2006; del Papa et al., 2013a; Pingel et al., 2016). From bottom to top, the Payogastilla Group has been subdivided into four litho-stratigraphic units (Fig. 2, Díaz and Malizzia, 1983; del Papa et al., 2013b): I) the Quebrada de los Colorados Formation (ca. 40–28 Ma, Payrola et al., 2009; DeCelles et al., 2011); II) the Angastaco Formation comprising the Tin Tin (ca. 28–15 Ma, del Papa et al., 2013a; Payrola et al., 2020) and Las Flechas (ca. 15–9 Ma, Carrapa et al., 2011; del Papa et al., 2013b; Pingel et al., 2016; Aramayo et al., 2017) members; III) the Palo Pintado Formation (ca. 9-5.2 Ma, Coutand et al., 2006; Bywater-Reyes et al., 2010; Pingel et al., 2016); and IV) the San Felipe Formation (ca. 5.2 to <1.9 Ma, Bywater-Reyes et al., 2010; Pingel et al., 2016). All these units are covered by coarse-grained Quaternary alluvial fans and fluvial sediments that characterize the present-day Calchaquí region (e.g., Strecker et al., 2007; Pingel et al., 2016).

The Malcante Range is located on the border between the Calchaquí region and the Lerma Valley (Figs. 1, 2B) and it is a high amplitude basement anticline composed primarily of the Puncoviscana Formation, bounded on the west by the Malcante fault. To the east of the Malcante Range in the Las Zanjas area, a minor anticline-syncline-anticline fold-train is defined by the Yacoraite Formation and the strata of the Santa Bárbara Subgroup and is truncated to the east by the Agua de Castilla fault (Fig. 2B).

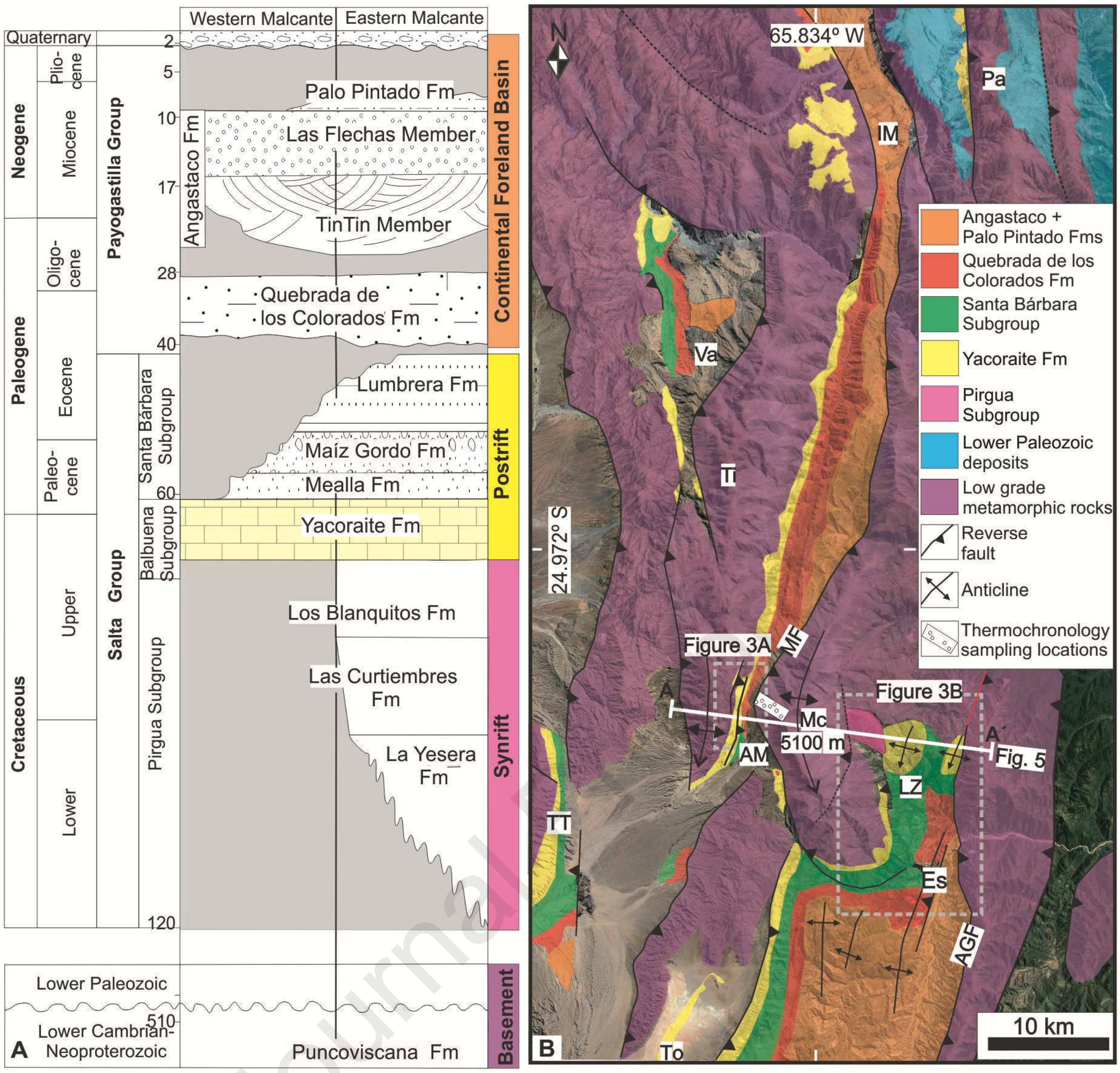

Fig. 2. A. Stratigraphy of the western flank of Malcante Range (AM) compared to the eastern flank (LZ) showing the stratigraphic position and lateral variability of stratigraphic units (based on Marquillas et al., 2005; del Papa et al., 2013b), **B.** Simplified geological map, highlighting the position of Cenozoic foreland deposits of the Eocene to Pleistocene Payogastilla Group in the Abra Malcante (AM) and Las Zanjas (LZ) areas (modified after Vergani and Starck, 1989). For location, see the white box in Figure 1. Specific areas and faults within the Calchaquí Region: TT-Tin Tin; To-Tonco; Es-Escoipe; Va-Vallecitos; IM-Ingeniero Mauri, Pa-Pascha; MF-Malcante fault; AGF-Agua de Castilla Fault. Legend code in the panel B, Fm: Formation. Lithology codes: Yacoraite Fm: limestones, Mealla Fm: sandstones, Maíz Gordo Fm: conglomeratic sandstones, Lumbrera: sandstones, Quebrada de los Colorados: sandstones and mudstones, Tin Tin Member: eolian sandstones, Las Flechas: conglomerates and sandstones, Palo Pinado: mudstones.

3. Methods

3.1 Sampling and structural reconstruction

We carried out detailed structural and geological mapping (1:10.000) along the western and eastern flanks of the Malcante mountain range, in the Abra Malcante and Las Zanjas areas, respectively (Fig.

3, 4 and 5). Lithostratigraphic units were identified by regional features and their stratigraphic contacts were mapped using contrasting lithofacies assemblages, changes in stratigraphic stacking patterns, and regional structural relationships. Our new data were supplemented by published sedimentological, structural and chronological data from adjacent areas (Vergani and Starck, 1989; González Villa, 2002; Salfity and Monaldi., 2006; Payrola et al., 2020).

A structural cross-section was constructed (Fig. 5) using Move software 2015.2 (academic license), based on measured field structural data projected onto a W-E transect (Fig. 2). The reconstruction of the Malcante fold utilizes a fault-propagation fold mechanism, modified by trishear deformation (Erslev, 1991, Hongn and Seggiaro, 2001; Payrola et al., 2020).

3.2 Thermochronological methods

Apatite (U-Th-Sm/He) thermochronology (AHe) is based on measuring the amount of helium produced by the radiogenic decay of ^{238}U, ^{235}U, ^{232}Th, and ^{147}Sm (e.g., Zeitler et al., 1987; Flowers et al., 2009). Apatites quantitatively retain helium at temperatures below ~40ºC. Between ca. 40 and 80°C, some helium is lost by diffusion; this interval is known as the PRZ-Partial Retention Zone (Wolf et al., 1998; Farley, 2000). The limits of the PRZ depend on cooling rate, grain shape and size, and the amount of alpha damage in the mineral lattice, which increases the apatite helium retentivity (e.g., Flowers et al., 2007; Gautheron et al., 2009; Brown et al., 2013). Damage effects can be identified by a correlation between effective uranium (eU=U + 0.235*Th) and age (Flowers et al., 2007; Flowers, 2009; Gautheron et al., 2009). AHe analyses (Table 1) were carried out at Potsdam University (alphachron) and in the German Research Center for Geoscience (GFZ) (ICP-MS). Details of the analytical methods are presented in Zhou et al. (2017) and in the supplementary material.

Apatite fission track (AFT) thermochronology is based on the quantification of mineral lattice damage (fission tracks), which are formed by the spontaneous fission of ^{238}U (e.g., Wagner et al., 1989). Tracks within the apatite mineral lattice can be partially annealed at temperatures between 60 and ~120°C, this interval is known as the Partial Annealing Zone (PAZ) (e.g., Fitzgerald et al., 1986). Resistance to annealing depends on mineral kinetics and composition. The length dimension of the intersection between the polished mineral surface and the tracks (Dpar) can be used as a proxy for the mineral resistance to annealing (Donelick et al., 1999; Ketcham et al., 1999). AFT analyses were conducted at the Thermochronology Laboratory La.Te.Andes (Salta, Argentina, Table 2). Track measurements were performed using a binocular microscope Zeiss® AXIO Imager Z2m and the Autoscan® software TrackWorks®. Unfortunately, very few confined track lengths were identified, and thus track lengths were not measured. Ages were calculated by the external detector method (Huford and Green, 1982, 1983; Wagner and van den Haute, 1992), and the data was processed using Trackkey© Software (Dunkl, 2002). Analytical details are provided in the supplementary data.

Thermochronology samples were collected from bedrock (Puncoviscana Formation) along a vertical transect of the western flank of the Malcante Range (for location, see Fig. 2 and Table 1). Due to the high degree of deformation present in the Puncoviscana Formation, structural and stratigraphic markers are not clear. Seven rock samples, each composed of three to five kilograms, were collected from 4,045 to 5,100 m a.s.l., according to the location of good outcrops.

3.3 Thermal modeling parameter and procedures

Rocks located at different positions within a coherent rock body experience similar thermal histories, where the temperature at different positions depends on the thermal gradient within the rock body (Gallagher et al., 2005). Temperature variations with depth are caused by the regional geothermal gradient; this may be perturbed locally by magmatism (e.g., Murray et al., 2018; Zapata et al., 2019b). In steep mountain belts formed by contractile-driven rock uplift, rocks at higher elevation experienced relatively lower temperatures compared to rocks at lower elevations throughout the thermal history, resulting in a positive relationship between elevation and cooling age (e.g., Fitzgerald and Malusà, 2019). Therefore, modern elevation can often be used as a proxy for the paleodepth. Herein, we present a multi-sample thermal history model from samples collected at different elevations along the Malcante Range. This model presents a single form of the thermal history based on samples collected in a contiguous basement block.

Thermal modelling was performed using QTQt software (v. 5.7.0 Gallagher, 2018), which uses a Bayesian transdimensional Markov chain Monte Carlo statistical approach to obtain the most probable thermal histories from multiple samples analyzed with thermochronological methods (Gallagher, 2012). The total number of iterations used in the sampling chain is equal to the burn-in + post-burn-in.

The burn-in is the number of initial iterations used to explore the model space; these initial interactions are discarded. After the burn-in stage, the post-burn-in is characterized by the number of iterations used in subsequent inferences of the thermal history. Several initial runs were performed in order to calibrate the model and select the best temporal intervals. Afterwards, model iterations were progressively increased until acceptance rates were below 0.5 and a stable plateau was observed in the likelihood chain. After 150,000 initial iterations (burn-in stage), the model was run for 350,000 iterations (post-burn-in stage).

We use the radiation damage model (RDAAM) from Flowers et al. (2009) for the AHe data and the annealing model from Ketcham et al. (2007) for the AFT data. Reproducible AHe ages were included in the model. We consider AHe ages to be reproducible when the 1 sigma interval of the distribution is less than 20% of the mean age (e.g., Flowers and Kelley, 2011; Zapata et al., 2019b). AHe single grain ages that fit the age-elevation trends and have possible eU controls were also included in the model despite not being reproducible. Such aliquots could have different closure temperatures and therefore may have significantly different ages. As a result, all aliquots were modeled because none of them was identified as an evident outlier following these criteria.

Geologically meaningful time-temperature constraints were included to improve the model output. To start the model with fully reset samples, we set the first constraint box above the temperature range of the PAZ at 580-520 Ma between 150 °C and 210 °C, the age of metamorphism of the Puncoviscana Formation (Hongn and Seggiaro, 2001; Aparicio González et al., 2010; Do Campo et al., 2013). To account for the prominent unconformity between the basement and the Cretaceous sediments of the Pirgua Subgroup, we set a surface temperature constraint between 80 and 60 Ma. The present-day surface temperature was set to 10 ± 10 °C.

We present the expected thermal history model, which is the weighted average of the accepted models, the expected model predicted ages, and the 2-sigma interval of the ages predicted by the accepted models. We allowed the model to have pre-Cenozoic thermal histories (70 ± 70 Ma) because one of the AFT ages is partially reset and to allow the model to consider radiation damage effects to better constraint single grain AHe closure temperatures. The chain of likelihood, the data used as constraints, and the parameters incorporated in the thermal models (Fig. 7) are presented in the supplementary data.

4. Results

4.1 Structural inventory

Field-based mapping and remote sensing analysis reveal that the flanks of the Malcante Range record complex structural relationships (unconformities, inverted strata, pinch outs, among others, Figs. 3 and 4). The field data support the interpretation that this range is an approximately north-south trending, asymmetrical basement-cored anticline bounded by the Tirao anticline and the Las Zanjas folds, to the west and east, respectively (Fig. 2). Its steeply southward plunging fold axis is well defined by the prominent limestones of the Yacoraite Formation, which were passively folded together with the underlying Puncoviscana bedrock (Fig. 4A). The fold has a width of 13,000 m, 5,000 m of vertical amplitude and an axial length of 27,000 m (Fig. 2), which makes it one of the largest basement anticlines in the Calchaquí area and the Lerma Valley to the east (Figs. 1 and 2).

The western limb of the Malcante Range is bounded by the west-vergent Malcante reverse fault, which uplifts the Puncoviscana basement over the Quebrada de los Colorados formations (Figs. 2 and 5). This fault has a curved trace to the south and continues towards the Escoipe creek with decreasing displacement (Fig. 3B).

Several outcrops within the footwall of the Malcante fault show a pronounced erosional unconformity between the Middle-Late Eocene Quebrada de los Colorados Formation and the Paleocene Mealla Formation (Santa Bárbara Subgroup) to the south (Abra Malcante) or between the Quebrada de los Colorados Formation and Yacoraite Formation (Balbuena Subgroup), north of the Abra-Malcante site (Figs. 3A and 4B). In addition, the Yacoraite Formation overlaps the Puncoviscana Formation in the eastern limb of the Tirao anticline. The only occurrence of Lower Cretaceous syn-rift strata of the Pirgua Subgroup is found within the eastern limb of the Malcante anticline in the Las Zanjas area (Fig. 3B).

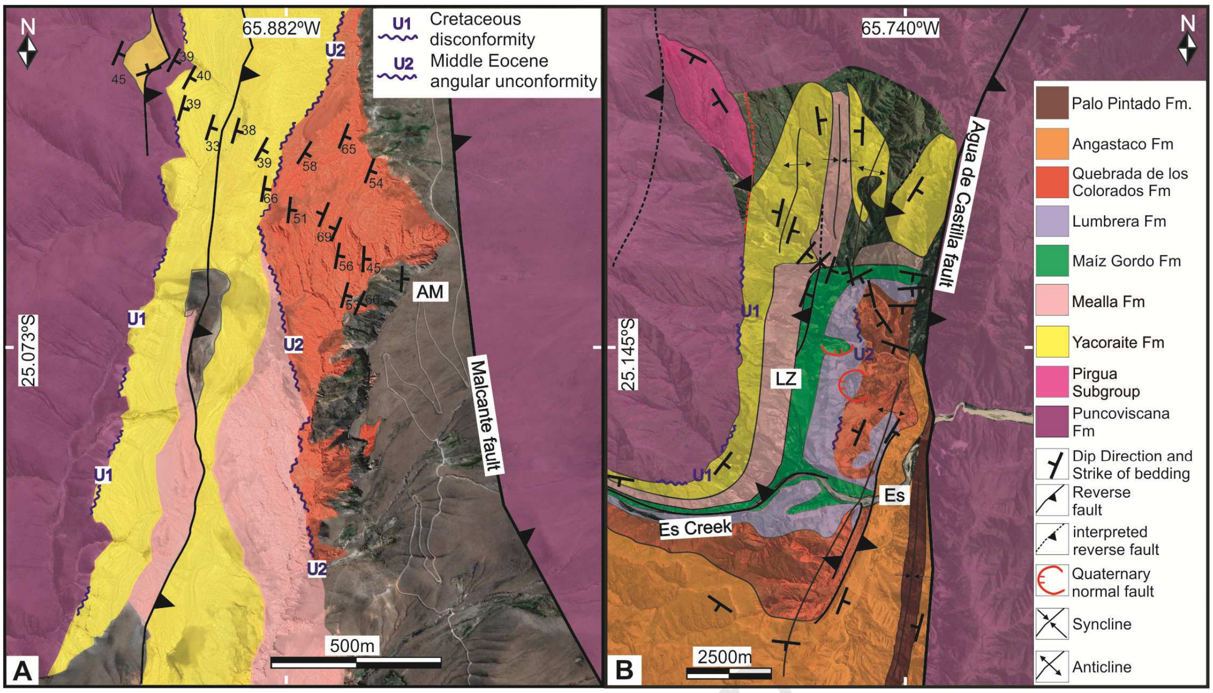

Fig. 3. Geological maps of the western limb (AM-Abra Malcante) and the eastern limb (Las Zanjas) of the Malcante anticline. **A.** Detailed map showing for the first time the unconformity (in red colour) between the Quebrada de los Colorados Formation and the Mealla Formation (U1) and the Yacoraite Formation (U2) in the Abra Malcante. **B.** Detailed map showing the complex structure of a thin belt of Pirgua syn-rift deposits, the post-rift deposits and the foreland Payogastilla Group in the Las Zanjas (LZ) and Escoipe (Es) areas.

The reconstruction of structures in the Las Zanjas area is challenging due to several reverse faults that displace the stratigraphy and because the outcrops are often covered by young deposits (Figs. 3B, 4C and D). However, we identified an anticline-syncline-anticline fold train. Moreover, we observed an angular unconformity that marks the contact between the Quebrada de los Colorados Formation and the Lumbrera Formation (Fig. 3B). Minor low-angle reverse faults, with east and west vergence, produce minor folds in the ductile levels of the Yacoraite and Maíz Gordo Formations (Fig. 4C). Finally, at the eastern border of the study zone, the west-vergent Agua de Castilla reverse fault uplifted the Puncoviscana Formation over the post-rift and Angastaco and Palo Pintado Formations foreland deposits (Fig. 3B). The Malcante basement block continues to the north up to the NW-SE-trending El Toro regional lineament and then continues to the Pascha Range. There, outside of the study area, multiple west-vergent reverse faults uplift the Puncoviscana Formation and lower Paleozoic strata (Fig. 2).

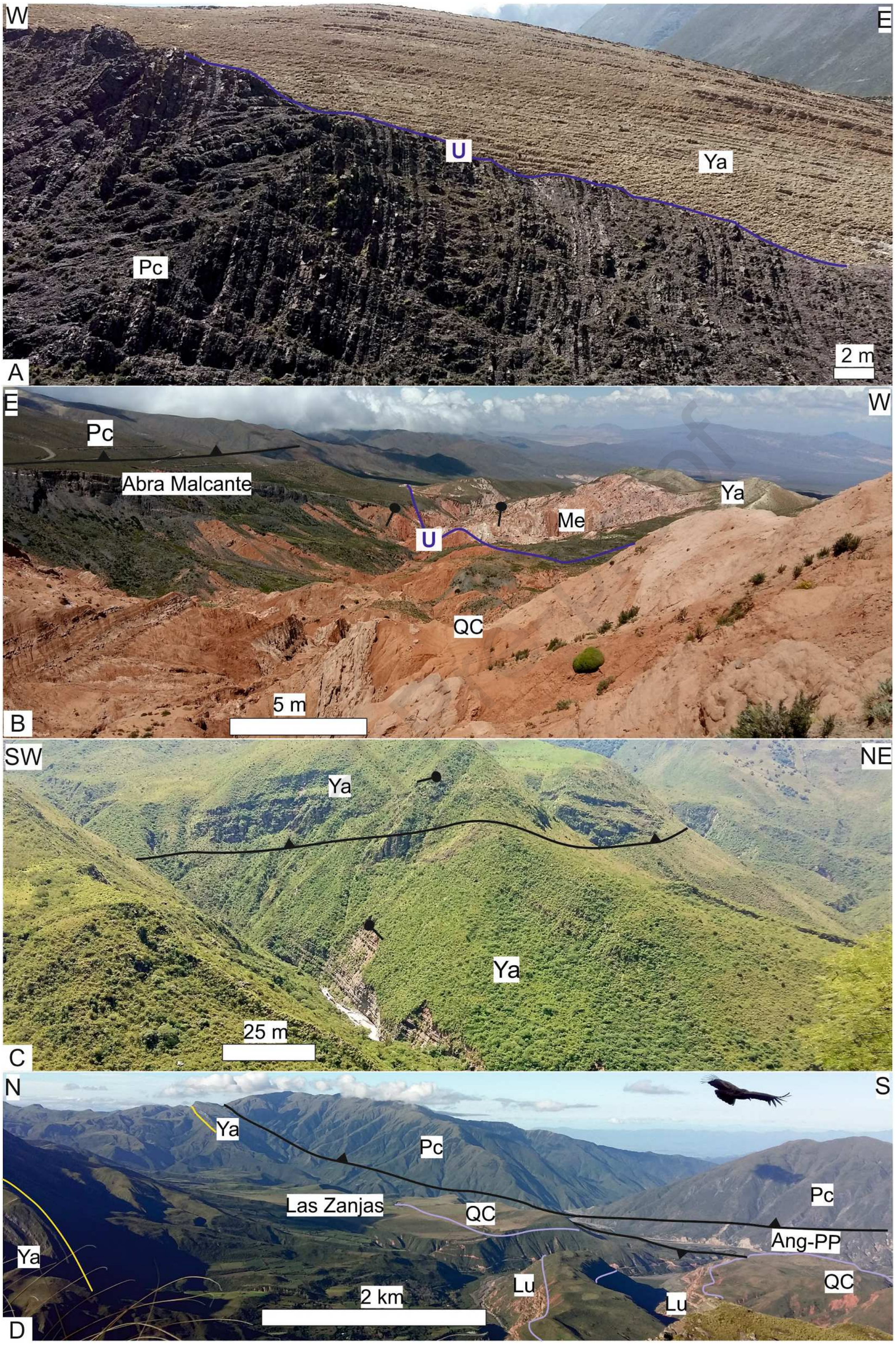

Fig. 4. A. Angular unconformity (U) between the Yacoraite Formation (Ya) and the Puncoviscana Formation (PC) in the footwall of the Malcante fault. **B.** Low angle unconformity (U) between the Quebrada de los Colorados Formation (QC) and the Mealla Formation (Me) in the Abra Malcante area. **C.** Minor reverse fault that duplicates the Yacoraite Formation in the northern part of the Las Zanjas area. **D.** Northeastern regional view of outcrops located between the eastern limb of the Malcante anticline and the Agua de Castilla reverse fault in the Las Zanjas area. Abbreviations: Lu-Lumbrera Formation, Ang-Angastaco Formation, PP-Palo Pintado Formation.

Based on field mapping, we reconstructed the possible fold geometry of the Malcante anticline, revealing a steep frontal limb and low-angle back-limb (Fig. 5). The geometry of the sedimentary cover allows us to project the dip domain to the basement in order to show the potential geometry of the anticline core. The cover was drawn in Fig. 5 with thickness intervals of 200 m. According to our structural reconstruction (Fig. 5), the Malcante reverse fault has a minimum of 1,400 m of reverse displacement. The sedimentary succession is thicker in the Las Zanjas area than the Abra Malcante area because to the assumption that there are unconformities over the crest of the Malcante anticline, consistent with unconformities described in this study and the regional data (Hongn et al., 2007; Carrera and Muñoz, 2013; Carrapa et al., 2011; Aramayo et al., 2017, Payrola et al., 2020). Details of the parameters used for the reconstruction are presented in the supplementary data.

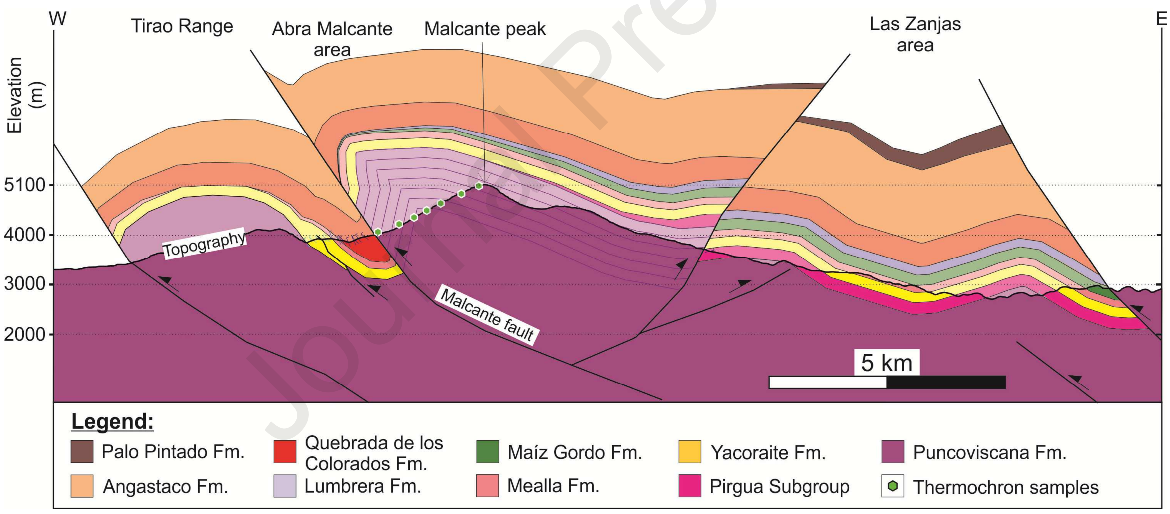

Fig. 5. West-east cross-section of the Malcante anticline and the Las Zanjas fold-train with the location of the samples analyzed by AHe and AFT (thermochron samples). Reconstruction based on field structural mapping using Move software. Erosion of the Santa Bárbara Subgroup in the crest of the anticline is based on the unconformity in the footwall of Malcante fault, and thinning of the foreland succession without Palo Pintado deposition over the crest of the anticline are assumed based on the AFT and AHe ages. Black lines represent reverse faults.

4.2 AHe and AFT results

We obtained 23 AHe single grain ages from seven bedrock samples from a vertical profile between 4,045 and 5,100 m elevation. AHe single grain ages range between ~4 and 10 Ma, with eU values between ~1 and 84 ppm, with the exception of one with 173 ppm, and equivalent spherical radius

(ESR) between ~36 and 131 µm. We obtained AFT ages from five of the samples. The four lowermost samples (PC1.2, PC2, PC2.1, and PC3.1) pass the Chi-square test and have overlapping ages between ~ 8 and 11.5 Ma and Dpar values between 1.8 and 2.1. Sample PC1.1, which is the highest of the samples with AFT data, did not pass the Chi-square test. This sample exhibits two discrete AFT grain-age populations, with central ages of 15.8 and 133.0 Ma. Analytical results for individual AHe single grain aliquots are presented in Table 1 and sample AFT data in Table 2.

Table 1: AHe data from the Malcante anticline

Sample	H (m)	Lat (° S)	Long (° W)	Stratigraphic unit	Stratigraphic age (Ma)	Grain	Raw Age (Ma)	AHe Age (Ma)	±1σ (Ma)	U (ppm)	Th (ppm)	147Sm (ppm)	eU	He (nmol/g)	Ft	ESR (µm)	Term.
PC1	5100	25.07458	65.85204	Puncoviscana	600-530	PC1-a	6.4	10.2	0.4	60	68	19	76	2.62	0.63	40	1
				Fm		PC1-b	3.5	5.1	0.5	9	22	32	14	0.27	0.68	47	2
						PC1-c	4.1	6.8	0.4	27	65	12	42	0.95	0.61	38	1
						PC1-d	4.2	6.5	0.3	29	34	41	37	0.84	0.64	42	1
						PC1-e	4.3	7.1	0.3	53	58	114	67	1.58	0.61	39	1
PC1.1	4900	25.07174	65.8569	Puncoviscana	600-530	PC1.1a	6.6	10.1	0.4	66	76	53	84	3.01	0.66	44	1
				Fm		PC1.1b	5.0	8.1	0.5	29	19	60	34	0.91	0.61	39	1
						PC1.1c	4.2	6.5	2.3	2	17	8	6	0.13	0.64	41	1
						PC1.1d	4.9	7.4	0.3	63	89	55	84	2.26	0.67	45	0
PC1.2	4740	25.07195	65.8594	Puncoviscana	600-530	PC1.2a	3.8	6.2	1.5	7	3	36	8	0.17	0.62	39	1
				Fm													
PC2	4551	25.07416	65.864	Puncoviscana	600-530	PC2-a	4.2	5.9	0.3	27	18	45	31	0.72	0.71	52	1
				Fm		PC2-b	4.1	4.6	0.1	7	2	1	7	0.16	0.88	122	1
						PC2-c	3.4	4.5	0.2	19	5	10	20	0.36	0.76	62	0
						PC2-e	3.7	5.3	2.8	1	6	1	2	0.04	0.70	49	1
PC2.1	4405	25.07115	65.8656	Puncoviscana	600-530	PC2.1a	3.9	6.1	0.4	41	124	25	70	1.47	0.63	41	0
				Fm													
PC3	4257	25.07061	65.8694	Puncoviscana	600-530	PC3-a	3.3	5.4	1.6	6	7	2	7	0.13	0.62	39	1
				Fm		PC3-b	5.0	7.0	0.1	30	146	14	65	1.78	0.73	55	1
						PC3-c	2.9	4.2	0.4	18	36	4	27	0.41	0.68	47	0
						PC3-e		3.6	2.6	4	10	4	7	0.07	0.57	35	0
PC3.1	4045	25.07572	65.8738	Puncoviscana	600-530	PC3.1a	7.0	9.2	0.5	3	13	6	6	0.24	0.76	62	0
				Fm		PC3.1b	4.1	6.1	0.1	134	166	29	173	3.80	0.67	45	0
						PC3.1c	3.9	6.4	0.4	36	95	65	59	1.26	0.61	39	0
						PC3.1d	3.9	6.6	1.0	19	9	32	21	0.46	0.59	37	0

Notes: Abbreviations: H, elevation; Lat, Latitude; Long, Longitude, AHe age, Corrected age, eU, effective Uranium, ESR, equivalent spherical radius, Term, Crystal terminations.

Table 2: AFT data from the Malcante anticline

Sample	H (m)	Lat (° S)	Long (° W)	n	*Rho* D	*N* D	Mean Dpar (μm)	±1σ (μm)	*Rho* s	*N* s	*Rho* i	*N* i	AFT Age (Ma)	±1σ (Ma)	P (χ2) (%)
PC1.1	4900	25.07174	65.8569	18	8.1	5000	1.79	0.24	1.76	102	5.34	310	133	37.3 (P1)	44
				7			1.81	0.23					15.8	5.1 (P2)	72
PC1.2	4740	25.07195	65.8594	35	7.2	5000	2.27	0.82	0.97	136	10.37	1460	11.5	1.4	49
PC2	4551	25.07416	65.864	19	7.3	5000	2.09	0.35	1.01	56	13.55	749	9.4	1.5	88
PC2.1	4405	25.07115	65.8656	27	7.4	5000	1.83	0.25	0.89	78	11.43	998	10.5	1.6	11
PC3.1	4045	25.07572	65.8738	37	8.2	5000	1.91	0.53	0.69	100	12.02	1724	8.2	1.0	21

Notes: AFT data from PC1.1 is divided into 2 populations, each of which passes the Chi-squared test. Abbreviations: H, elevation; Lat, Latitude; Lon, Longitude; n, number of analized crystals; RhoD, dosimeter density; Dpar, pit diameter of tracks; *N*s, number of spontaneous track; ρ_s, spontaneous track density (x 10^5 cm^{-2}), *N*i, number of induced track; ρ_i, induced track density; P (X^2), Chi-squared test. Zeta-value 330.4 ± 20.2 obtained by the analyst (Guadalupe Arzadum) using IRMM 540 dosimetry glasses. Sample etching conditions (HNO_3) 5.5 N for 20' at 20ºC.

Thermochronologic data derived from a vertical transect can be readily evaluated for changes in cooling trends. The apparent exhumation rate can be determined from a plot of AHe or AFT ages versus elevation when the samples are considered to be fully reset (e.g., Fitzgerald et al., 1986). The AFT data on figure 6 show a positive correlation between elevation and age. The young ages of the 4 lower AFT samples are interpreted to reflect fully reset ages. In contrast, the 2 populations with central ages of 133.0 and 15.8 Ma from the highest sample (PC1.1) suggest that the sample has not been hotter than the AFT closure temperature during the Cenozoic. Therefore, the bottom of a fossil PAZ is placed below this sample, suggesting that there was an increase in the exhumation rate at ~11 Ma.

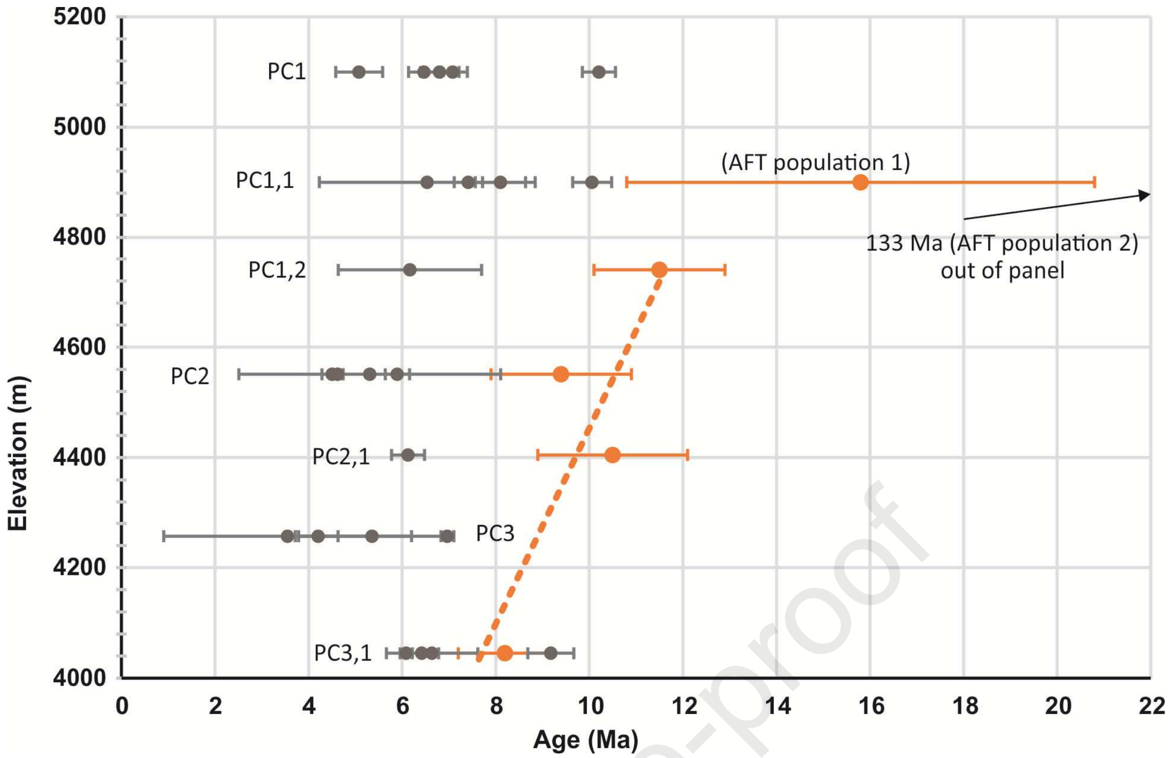

Fig. 6 AFT and AHe cooling age plotted vs. elevation of PC samples, showing regression line (dashed) whose slope indicates the apparent exhumation rate. Grey dots represent AHe single grain ages. Orange dots represent AFT ages. The exhumation rate yields ~0.2 ± 0.1 km/Ma from the AFT regression line with a $R^2 = 0.73$ (calculated without the partial reset sample PC1.1).

4.3 Thermal history modeling results

We included all 23 AHe single grain ages in our QTQt model because they pass the criteria presented in the methodology section. Twelve aliquots from samples PC1.1, PC2, and PC3.1 were included because they exhibit intra-sample reproducibility. Nine aliquots from samples PC1 and PC3 were included because they exhibit a positive correlation between eU and age (Table 1). Although samples PC1.1 and PC2.1 each had only a single aliquot AHe age, these two aliquots were included because they overlap with the AHe ages from the samples above and below (Table 1). The PC3.1b aliquot (in the lower sample) with high concentration of U was included because could indicate the maximum temperature reached.

AFT data from five samples were included in the model. Although the two grain age populations from sample PC1.1 show similar Dpar values, the populations were modelled separately as Dpar does not account for all possible kinetic differences among the grains (e.g., Ketcham et al., 1999). Unfortunately, we do not have information about wt% Cl from our samples. Since QTQt can resample

Dpar values during the iterations to improve the fit of the data (Gallagher, 2012), we have modeled both AFT-age populations to test if the observed age dispersion can be explained by different mineral kinetics.

Figure 7A shows the expected multi-sample thermal history of samples arranged according to present-day elevations. The Max likelihood chain is shown in the supplementary data. This model exhibits pre-80 Ma cooling, followed by Late Cretaceous to Miocene reheating up to 100°C and final cooling between ca. 10 Ma and the present. In this model, the 23 AHe aliquots are adequately predicted, including the two different AFT age populations of sample PC1.1. As expected, the model predicts different Dpar values for each population. Predicted AFT ages for the lowermost sample are at least 2 Ma older than the observed age. The model successfully predicts the remaining AFT ages (Fig. 7C).

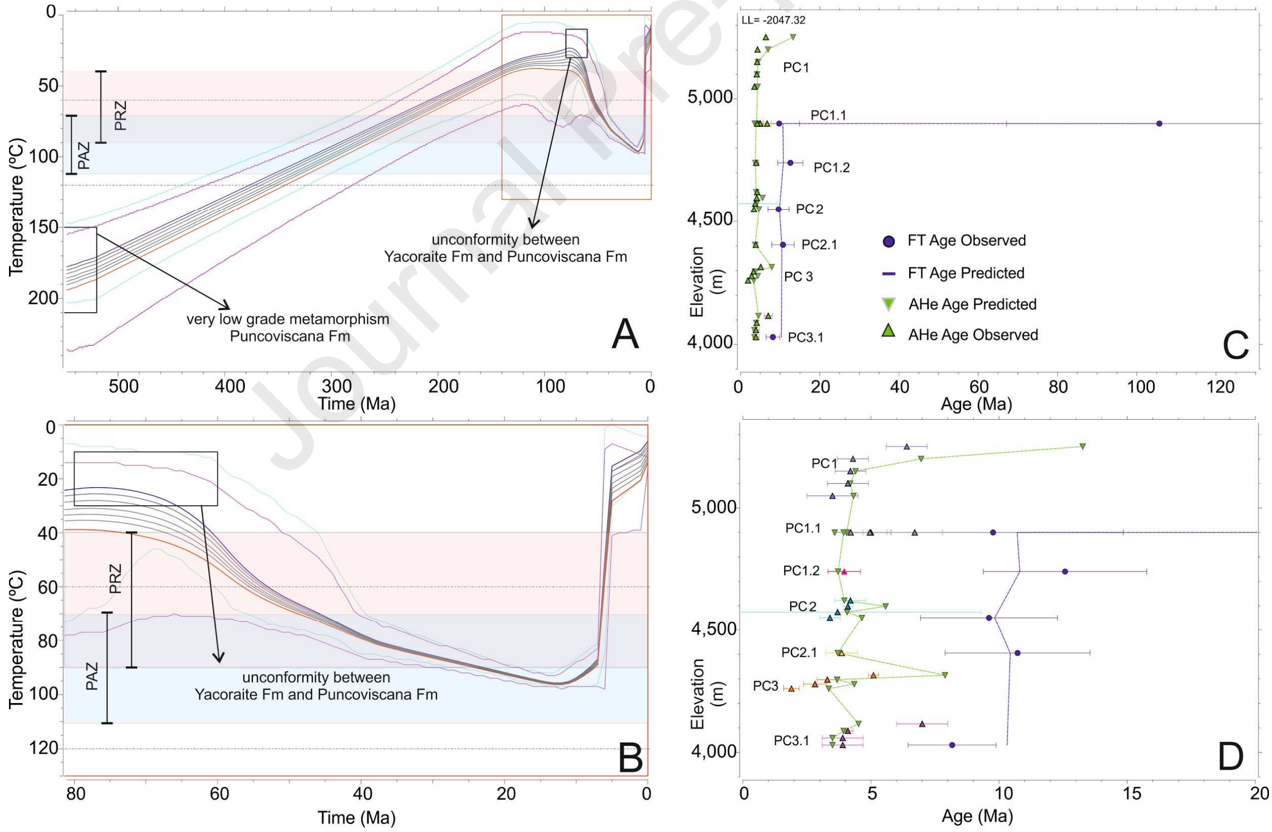

Fig. 7. A. The expected multi-sample thermal model, showing the uppermost and the lowermost sample thermal histories plotted in blue and red, respectively. The thermal histories for all intervening samples are drawn in grey. For the uppermost sample, the 95% credible intervals are drawn in light blue and these reflect the uncertainty in the inferred thermal history alone. For the lowermost sample, the 95% credible intervals are drawn in magenta and these reflect the combined uncertainty in the inferred thermal history and also the offset parameters. Light blue and light pink shaded areas represent the apatite partial annealing zone and apatite partial retention zone. **B.** Detail of the last 80

Ma from 0 and 130ºC of the thermal model. **C.** Comparison of observed AHe-AFT ages versus those predicted by the thermal model, **D.** Magnified version of the C panel, highlighting the last 20 My. Legend: blue dots-fission track ages observed, blue line-fission track predicted, colours triangles-AHe ages observed, green inverted triangles-AHe ages predicted.

5. Discussion

5.1 Exhumation analysis of the Malcante Range

According to the regional thickness of the sedimentary post-rift and foreland strata, sample PC1.1 (4,900 m a.s.l.) must have been buried beneath at least 2,700 m of strata. Our structural interpretation suggests that about 500 m of basement was removed by erosion; therefore, this sample was buried by ~3,200 m. The multi-sample thermal history model shows that the upper sample experienced a maximum temperature of ~95°C at ~11 Ma. Considering a mean annual surface temperature of 10°C, this implies a paleo-geothermal gradient ~27ºC/km for the late Miocene, which is higher than the estimates for the Payogastilla Group in the Angastaco Basin to the southeast of the study area (18 ± 8º C/km at 16/15 Ma, Deeken et al., 2006). Moreover, if the upper sample was at 3,200 m depth at 10 Ma, this would imply an average exhumation rate of ~0.3 ± 0.5 km/Ma, possibly faster than the ~0.2 ± 0.1 km/Ma apparent exhumation rate predicted from the age-elevation plot (Fig. 6). Two possible explanations for these observations are that i) the amount of burial could be significantly underestimated or that ii) the rock column could have been rotated about a horizontal axis during exhumation, such that the samples now span a smaller range of elevation than when they cooled through the apatite PAZ and PRZ.

During the growth of the significant hanging-wall anticline, the Malcante Range experienced a transition from the erosion of structurally shallow, easily-eroded sediment to the erosion of structurally deeper, more resistant basement lithologies. The contrast in rock erodibility between the basement and the overlying sedimentary strata may have resulted in faster initial exhumation rates and reduced surface uplift during the erosion of the sedimentary cover, followed by slower exhumation rates and increased surface uplift after the basement was exposed; thus, the bulk of the surface uplift of the Malcante Range probably occurred during the final stages of the exhumation. The majority of the present 3,000 m of relief was likely formed after the removal of much of the ~2,700 m thick post-rift and foreland-basin sedimentary sequences, when the more resistant Puncoviscana Formation was exposed. Similar relationships between rock erodibility, exhumation, and surface uplift have been documented in other segments of the Central Andes (Sobel and Strecker, 2003; Zapata et al., 2019b).

A significant rock column was exhumed between 10 and 0 Ma. Provenance studies on the Palo Pintado Formation (10-5 Ma) in the Escoipe area, to the southeast, did not reveal the exhumation of the post-rift Yacoraite Formation (Gonzalez Villa, 2002). Therefore, we suggest that the erosion products from the exhumed Malcante Range could have been transported farther east, out of the Calchaquí Basin and possibly deposited in the late Miocene-Pliocene conglomerate sequence in the adjacent Lerma Valley which contains eastward-directed paleocurrent indicators (Hain et al., 2011); this hypothesis should be corroborated in future studies.

5.2 Fault reactivation history

The thin sequence of syn-rift strata (Pirgua Subgroup) in the Las Zanjas area, on the eastern flank of the Malcante anticline, and the basement unconformity below the Yacoraite Formation to the west and south (Abra de Malcante and Escoipe areas, Figs. 2 and 3) indicate a westward pinch-out of the Pirgua deposits. This in turn supports the notion of a gently eastward-sloping paleotopography during the Early Cretaceous. The unconformity between the marine deposits of the Yacoraite and Puncoviscana formations implies that the area was at sea level during the Maastrichtian marine transgression (Marquillas et al., 2005).

From the Cretaceous to the Eocene, this region was a depocenter controlled by thermal subsidence, represented by the final post-rift deposits of the Balbuena and Santa Bárbara Subgroups (Mealla, Maíz-Gordo, and Lumbrera formations) (Marquillas et al., 2005). Subsequently, the Payogastilla Group was deposited in a foreland-basin setting (e.g., Starck and Vergani, 1989; Díaz and Malizzia, 1983; Coutand et al., 2006; Payrola et al., 2009). The first stage of Malcante structural growth is defined by the low-angle unconformity between the Quebrada de los Colorados Formation and the Mealla/Yacoraite formations, highlighting a phase of middle-late Eocene deformation that caused the erosion of the 300-m-thick Santa Bárbara Subgroup from the western limb of the Malcante anticline (Fig. 3). Unfortunately, the expected thermal effect of this erosion would be ~5 to 8°C, too small to be recorded by our thermochronological data or a thermal history.

The middle Oligocene - middle Miocene Angastaco Formation records local angular unconformities linked to several deformation events in the Calchaquí region (Carrera and Muñoz, 2008; Carrapa et al., 2012; Aramayo et al., 2017; Payrola et al., 2020; Fig. 2A). The decrease in the thickness of this unit in the western limb of the Malcante anticline (northern part) could be related to the reactivation of the Malcante fault during the middle Miocene, which is consistent with the unconformities recorded in the Tonco valley (Payrola et al., 2020) and the Quebrada de Carachi - El Toro (Pearson et al., 2013; Montero-López et al., 2017). Our modeled thermal history between 35 and ca. 10 Ma indicates a relatively long subsidence period in the region (Fig. 7), which is necessary to accumulate the foreland deposits. The thermal model constrains the beginning of the cooling/exhumation event at ~10 Ma (Fig. 7). This exhumation must be related to episodes of Malcante fault reactivation as deduced from mapped unconformities in the Malcante anticline, as well as episodes of faults reactivation recorded in the regional Miocene basin strata (Fig. 8A, Carrera and Muñoz, 2013; Pearson et al., 2013; Payrola et al., 2020).

This late Cenozoic cooling event is regionally consistent with the ca. 10 Ma AHe cooling ages obtained from the neighboring Tin-Tin (5.7 - 11.9 Ma), Angastaco (9.9 - 10.6 Ma), Amblayo-Agua de Castilla (8 - 12 Ma), and Sierra de los Colorados (5.7 - 9.9 Ma) sections, farther southwest (Fig. 8A; Carrapa et al., 2011; Kortyna et al., 2019; Payrola et al., 2020). In addition, thermochronological data (especially AHe ages) from the Malcante Range and other neighboring mountain ranges (Fig. 8A) (from north to south, the Pascha-Lesser (5.2 - 12.1 Ma, Pearson et al., 2013), Malcante (4.2 - 10.2 Ma, this study), Tonco-Filos del Pelado (7.4 - 17.1, Payrola et al., 2020), and Agua de Castilla ranges (8 - 12 Ma, Kortyna et al., 2019)), could indicate a concentration of shortening in a relatively narrow north-south trending deformation belt. Our study area presently receives ~300 mm of mean annual precipitation (Noe et al., 2012). It is possible that the establishment of the South American low-level jet (e.g., Vera et al., 2006) at 10-7 Ma (Strecker et al., 2007; Mulch et al., 2010; Rohrmann et al., 2016) could have contributed to the 7 and 5 Ma accelerated exhumation of the Malcante Range (based on the thermal model) by increasing the available precipitation in this area. A more humid setting at this time is indicated by isotopic data and fossils from the Palo Pintado Formation in other areas (Pingel et al., 2016; Rohrman et al., 2016). After 5 Ma, the exhumation of less erodible bedrock must have facilitated the development of high topography, which is consistent with surface uplift estimates obtained from intermontane basins in this region (Rohrmann et al., 2016; Pingel et al., 2016, 2020).

On the other hand, pre-Cenozoic basement structures can be reactivated more easily than new faults can be created (Masek and Duncan, 1998; Hilley and Strecker, 2004; Yagupsky et al., 2014). The Malcante retrovergent fault could be a pre-Andean heterogeneity that was reactivated during the Cenozoic, as suggested by the west-vergence of this fault and the absence of Cretaceous or Paleozoic units in the surrounding area. This >5,000-m high structural system could have accumulated a large amount of shortening during the Cenozoic, defining part of a zone of concentrated deformation which includes the Luracatao, Cachi, Calchaquí and Malcante fault zones (Fig. 8A), where basement with different metamorphic grades was uplifted; deeper crustal levels were exhumed in the north than in the south (Hongn et al., 2010; Payrola et al., 2012; Pearson et al., 2012; Payrola et al., 2020).

The 5,100-m high Malcante Range is located in an area with reduced rainfall, to the west of an orographic barrier which does not exceed 4,200 m in the heavily vegetated Yungas green belt (Fig. 1B). The position of this anomalously high range (Fig. 8B) could be related to the west-east regional balance of shortening. Figure 8 depicts a southward decrease of the topography, visualized along three west-east transects. The number of significant Cenozoic thrust faults also varies between profiles. The northern transect (1) crosses the Cachi, San Miguel, and Tirao high altitude basement blocks, which have absorbed a large amount of Cenozoic fault-displacement in three well-defined zone of concentrated deformation (Hongn and Seggiaro, 2001; Payrola et al., 2012, Pearson et al., 2012 and 2013). In contrast, the two southern transects depict a relative decrease in the topography, which is interpreted to reflect a decrease of fault-displacement along individual structures that is compensated by an increase in the number of regional faults in order to balance the regional crustal shortening (Salfity and Monaldi, 2006; Carrera and Muñoz, 2013; Payrola et al., 2020).

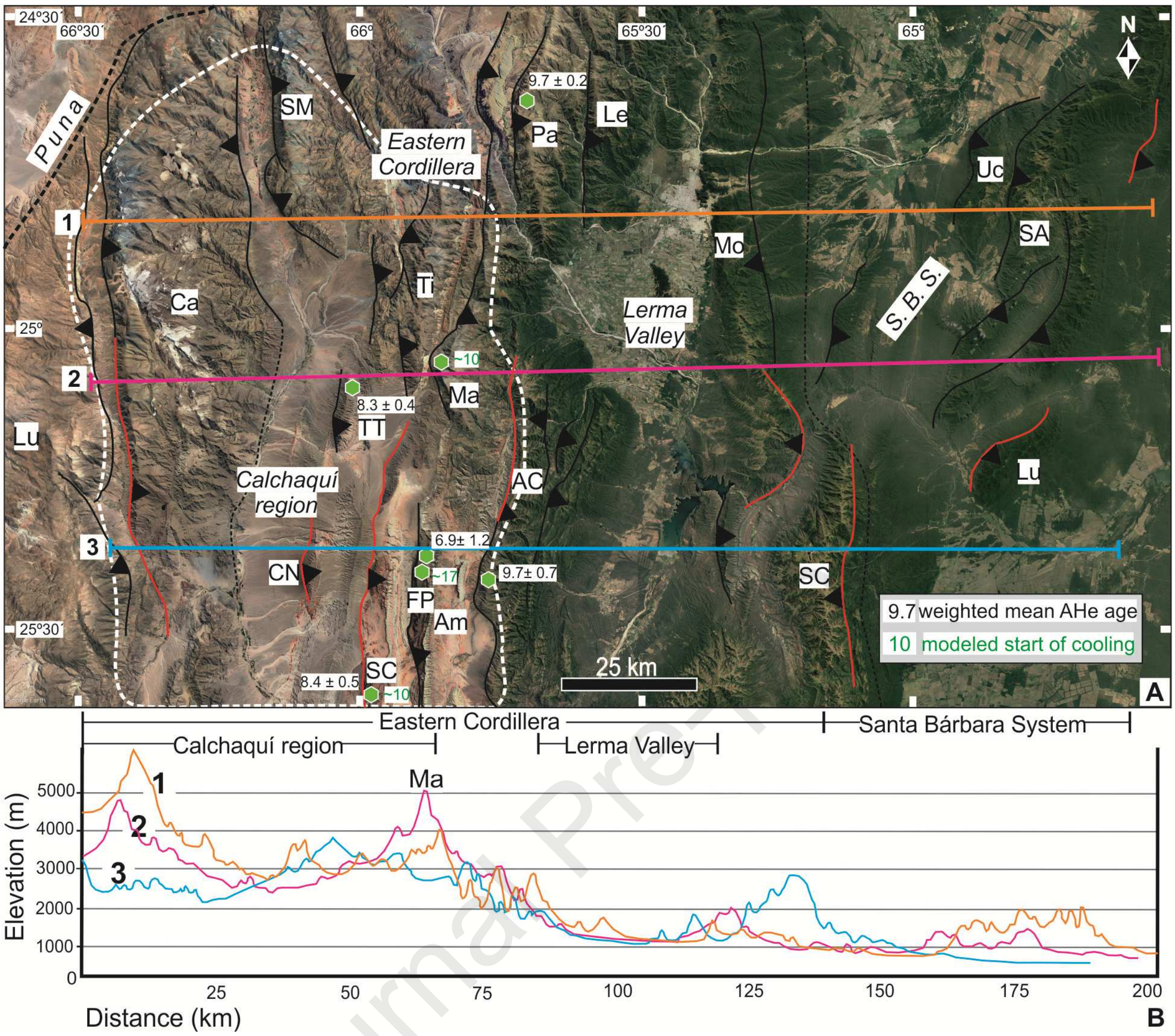

Fig. 8. A. Google Earth satellite image of the southern Eastern Cordillera and northern Santa Bárbara System (S.B.S.) showing location of AHe ages (Carrapa et al., 2011; Pearson et al., 2013, Kortyna et al., 2019; Payrola et al., 2020). Main reverse faults shown in black, Cretaceous inverted faults in red; major mountains ranges are labelled (Lu Cumbres de Luracatao, Ca Cachi, SM San Miguel, CN Cerro Negro, TT TinTin, Ti Tirao, Ma Malcante (this study), SC Sierra de los Colorados, FP Filos del Pelado-Tonco, Am Amblayo, AC Agua de Castilla, Pa Pascha, Le Lesser, Mo Mojotoro, SC Crestón, Uc Unchime, SA San Antonio, Lu Lumbrera). Dashed white lines mark the borders of the Payogastilla Group basin, coincident with the borders of Calchaquí region. Dashed black lines show the borders between main morphostructural units. **B.** Three topographic profiles showing the southward and eastward decrease of altitude. Location of profiles is shown in panel A. Note the higher altitude of the Malcante Range in profile 2 compared to the other ranges in this position along strike.

6. Conclusions

The basement anticline Malcante Range was uplifted by a retrovergent reverse fault. Based on our structural reconstructions, this fault has a minimum Cenozoic displacement of 1,400 m. The significant unconformity between the Quebrada de los Colorados Formation and Yacoraite Formation, located on the western limb of the Malcante anticline, delineates the first episode of faulting during the middle Eocene. About 2,700 m of strata were deposited between the late Eocene and ca. 10 Ma. AFT and AHe data from a vertical profile across the Malcante Range suggest a period of rock uplift and efficient erosion that started around 11 Ma. This exhumation event was related to erosion of soft sedimentary cover during the formation of the actual Malcante orographic barrier, which separates the humid climate in the Lerma Valley from the semi-arid climate in the northern Calchaquí region, possibly during the Plio-Pleistocene. The Puncoviscana basement is now exposed in the core of the range; we suggest that exposure of this more erosionally-resistant lithology may have been responsible for significant surface uplift of the Malcante Range during the Plio-Pleistocene.

The anomalously high altitude of the Malcante Range compared to other ranges in similar structural positions along the eastern border of the Calchaquí region could be related to the accommodation of late Miocene-Pliocene shortening along only a few faults compared to a larger number of Cenozoic faults which uplift the basement-cored ranges to the north and south. Concentrating deformation along only a few structures could facilitate a higher amount of rock uplift in the Malcante Range. Thus, high elevation was related to the compensation of east-vergent shortening linked to the availability of pre-existing basement structures, which could have been reactivated during the Cenozoic.

Acknowledgments

This work was supported by PICT 2245-15, Strategy CONICET Potsdam University, PICT 2016-1274 grants. CONICET-La.Te. Andes are thanked for AFT analytical results. Additional support came from DFG grant STR 373/34-1 and the Brandenburg Ministry of Sciences, Research and Cultural Affairs, Germany, within the framework of the international research training group IGK2018 SuRfAce processes, TEctonics and Georesources: The Andean foreland basin of Argentina (StRATEGy). We also acknowledge the support for S. Zapata from the MST-STRI Bytnar Postdoctoral Fellowship. We thank the Colque family from the foothills of the Malcante Range for their kindness and hospitality during our fieldwork and the Administración de Parques Nacionales and its guards for granting access to the Parque Nacional Los Cardones. Carolina Montero and Francisco

Figueroa collaborate during the fieldwork. We are also grateful to V. García and F. Hongn for constructive and motivating discussions.

References

Allmendinger, R.W., Victor, V.A., Jordan, T.E., Palma, M., Isacks, B.L., 1983. Paleogeography and Andean structural geometry, Northwest Argentina. Tectonics, 2, 1–16.

Aparicio Gonzalez, P. A, Moya, M. C., Impiccini, A. 2010. Geology Published. Estratigrafía de las rocas metasedimentarias (Neoproterozoico-Cámbrico) de la Sierra de Mojotoro, Cordillera Oriental Argentina.

Aramayo, A., Guzmán, S., Hongn, F., del Papa, C., Montero-López, C., Sudo, M., 2017. A Middle Miocene (13.5–12 Ma) deformational event constrained by volcanism along the Puna-Eastern Cordillera border, NW Argentina. Tectonophysics, 703–704, 9–22. https://doi.org/10.1016/j.tecto.2017.02.018.

Ballato, P., Brune, S., Strecker, M.R., 2019. Sedimentary loading–unloading cycles and faulting in intermontane basins: insights from numerical modeling and field observations in the NW Argentine Andes. Earth Planet. Sci. Lett. 506, 388–396.

Barazangi, M., Isacks, B., 1976. Spatial distribution of earthquakes and subduction of the Nazca plate beneath South America. Geology, 4, 686–692.

Beaumont, C., Fullsack, P., Hamilton, J., 1992. Erosional control of active compressional orogens, in: Thrust Tectonics. pp. 1–18. https://doi.org/10.1007/978-94-011-3066-0_1.

Bookhagen, B., Strecker, M.R., 2012. Spatiotemporal trends in erosion rates across a pronounced rainfall gradient: Examples from the southern Central Andes. Earth Planet. Sci. Lett. 327–328, 97–110. https://doi.org/10.1016/j.epsl.2012.02.005.

Brown, R.W., Beucher, R., Roper, S., Persano, C., Stuart, F., Fitzgerald, P., 2013. Natural age dispersion arising from the analysis of broken crystals. Part I: Theoretical basis and implications for the apatite (U-Th)/He thermochronometer. Geochim. Cosmochim. Acta 122, 478–497. https://doi.org/10.1016/j.gca.2013.05.041.

Burbank, D.W., Bookhagen, B., Gabet, E.J., Putkonen, J., 2012. Modern climate and erosion in the

Himalaya. C. R. Geosci.344, 610–626. https://doi .org /10 .1016 /j .crte .2012 .10 .010.

Burtman, V.S., 1975. Structural geology of Variscan Tien Shan, USSR. Am. J. Sci., Ser. A 275, 157–186.

Buiter, S.J.H., Adrian Pfiffner, O., 2003. Numerical models of the inversion of half-graben basins. Tectonics, 22-5, 1057. https://doi.org/10.1029/2002TC001417.

Bywater-Reyes, S., Carrapa, B., Clementz, M., Schoenbohm, L., 2010. Effect of late Cenozoic aridification on sedimentation in the Eastern Cordillera of northwest Argentina (Angastaco basin). Geol. Soc. Am., 38, 235–238. https://doi.org/10.1130/G30532.1.

Carrapa, B., and DeCelles, P.G., 2008. Eocene exhumation and basin development in the Puna of northwestern Argentina. Tectonics, 27. https://doi.org/10.1029/2007TC002127.

Carrapa, B., Trimble, J.D., Stockli, D.F., 2011. Patterns and timing of exhumation and deformation in the Eastern Cordillera of NW Argentina revealed by (U-Th)/He thermochronology. Tectonics 30, n/a-n/a. https://doi.org/10.1029/2010TC002707.

Carrapa, B., Bywater-Reyes, S., DeCelles, P.G., Mortimer, E., Gehrels, G.E., 2012. Late Eocene-Pliocene basin evolution in the Eastern Cordillera of northwestern Argentina (25°-26°S): Regional implications for Andean orogenic wedge development. Basin Res. 24, 249–268. https://doi.org/10.1111/j.1365-2117.2011.00519.x.

Carrera, N., Muñoz, J.A., 2008. Thrusting evolution in the southern Cordillera Oriental (northern Argentine Andes): Constraints from growth strata. Tectonophysics, 459, 107–122. https://doi.org/10.1016/j.tecto.2007.11.068.

Carrera, N., Muñoz, J.A., Roca, E., 2009. 3D reconstruction of geological surfaces by the equivalent dip-domain method: An example from field data of the Cerro Bayo Anticline (Cordillera Oriental, NW Argentine Andes). J. Struct. Geol. 31, 1573–1585. https://doi.org/10.1016/j.jsg.2009.08.006.

Carrera, N., Muñoz, J.A., 2013. Thick-skinned tectonic style resulting from the inversion of previous structures in the southern Cordillera Oriental (NW Argentine Andes). Geol. Soc. Spec. Publ. 377, 77–100. https://doi.org/10.1144/SP377.2.

Coutand, I., Cobbold, P.R., de Urreiztieta, M., Gautier, P., Chauvin, A., Gapais, D., Rossello, E.A., López-Gamundí, O., 2001. Style and history of Andean deformation, Puna plateau, northwestern Argentina. Tectonics, 20(2), 210-234.

Coutand, I., Carrapa, B., Deeken, A., Schmitt, A.K., Sobel, E.R., Strecker, M.R., 2006. Propagation of orographic barriers along an active range front: Insights from sandstone petrography and detrital apatite fission-track thermochronology in the intramontane Angastaco basin, NW Argentina. Basin Res. 18, 1–26. https://doi.org/10.1111/j.1365-2117.2006.00283.x.

Dataset: © JAXA/METI ALOS PALSAR L1.0 2010. Accessed through ASF DAAC 08 May 2020.

Dahlen, F.A., 1990, Critical taper model of fold-and-thrust belts and accretionary wedges: Annual Review of Earth and Planetary Sciences, 18, 55–99. doi:10.1146/annurev.ea.18.050190.000415.

Davis, D., Suppe, J., Dahlen, F.A., 1983. Mechanics of fold-and-thrust belts and accretionary wedges. J. Geophys. Res. 88 (NB2), 1153–1172.

Decelles, P.G., Carrapa, B., Horton, B.K., Gehrels, G.E., 2011. Cenozoic foreland basin system in the central Andes of northwestern Argentina: Implications for Andean geodynamics and modes of deformation. Tectonics 30, 1–30. https://doi.org/10.1029/2011TC002948.

Deeken, A., Sobel, E.R., Coutand, I., Haschke, M., Riller, U., Strecker, M.R., 2006. Development of the southern Eastern Cordillera, NW Argentina, constrained by apatite fission track thermochronology: From early Cretaceous extension to middle Miocene shortening. Tectonics, 25. https://doi.org/10.1029/2005TC001894.

del Papa, C.E., Hongn, F., Powell, J., Payrola, P., Do Campo, M., Strecker, M.R., Petrinovic, I., Schmitt, A.K., Pereyra, R., 2013a. Middle Eocene-Oligocene broken-foreland evolution in the Andean Calchaqui Valley, NW Argentina: Insights from stratigraphic, structural and provenance studies. Basin Research, 25, 574–593. https://doi.org/10.1111/bre.12018.

del Papa, C.E., Hongn, F.D., Payrola, P.A., Powell, J., Deraco, V., Herrera, C., 2013b. Relaciones estratigráficas de las Formaciones Quebrada de los Colorados y Angastaco (Paleógeno-Neógeno), Valles Calchaquíes, Salta (Argentina): Significado en el análisis de la cuenca del Grupo Payogastilla. Lat. Am. J. Sedimentol. Basin Anal. 20, 51–64.

Díaz, J.I., Malizzia, D. 1983. Estudio geológico y sedimentológico del Terciario Superior del valle Calchaquí, Salta. Boletín Sedimentológico, 2, 8-28.

Do Campo, M., Collo, G., Nieto, F. 2013. Geothermobarometry of very low-grade metamorphic pelites of the Vendian–Early Cambrian Puncoviscana Formation (NW Argentina). European Journal of Mineralogy, 25(3), 429–451.

Donelick, R.A., Ketcham, R.A., Carlson, W.D., 1999. Variability of apatite fission-track annealing kinetics: II. Crystallographic orientation effects. Am. Mineral. 84, 1224–1234. https://doi.org/10.2138/am-1999-0902.

Dunkl, I., 2002. Trackkey: A windows program for calculation and graphical presentation of fission track data. Comput. Geosci. 28, 3–12. https://doi.org/10.1016/S0098-3004(01)00024-3.

Erslev, E.A., 1991. Trishear fault-propagation folding. Geology, 19, 617–620. https://doi.org/10.1130/0091-7613(1991)019<0617.

Escayola, M.P.; van Staal, C.R.; Davis, W.J., 2011. The age and tectonic setting of the Puncoviscana Formation in northwestern Argentina: An accretionary complex related to Early Cambrian closure of the Puncoviscana Ocean and accretion of the Arequipa-Antofalla block. Journal of South American Earth Sciences, 32(4), 438-459.

Espinoza, N., Melchor, R.N., del Papa, C., 2020. Sand pipes in eolian deposits as recorders of Andean deformation in the Miocene Angastaco Formation, northwest Argentina. Journal of South American Earth Sciences, 103, https://doi.org/10.1016/j.jsames.2020.102730.

Farley, K.A., 2000. Helium diffusion from apatite: general behavior as illustrated by Durango fluorapatite. Journal of Geophysical Research, 105, 2903–2914.

Fitzgerald, P.G., Sandiford, M., Barrett, P.J., Gleadow, A.J.W., 1986. Asymmetric extension associated with uplift and subsidence in the Transantarctic Mountains and Ross Embayment. Earth Planetary Science Letters, 81, 67–78. https://doi.org/10.1016/0012-821X(86)90101-9.

Fitzgerald, P.G., Malusà, M.G., 2019. Concept of the Exhumed Partial Annealing (Retention) Zone and Age-Elevation Profiles in Thermochronology, in: Fission-Track Thermochronology and Its Application to Geology, Springer Textbooks in Earth Sciences, Geography and Environment. Springer International Publishing, pp. 165–189. https://doi.org/10.1007/978-3-319-89421-8.

Flowers, R.M., Shuster, D.L., Wernicke, B.P., Farley, K.A., 2007. Radiation damage control on apatite (U-Th)/He dates from the Grand Canyon region, Colorado Plateau. Geology, 35, 447–450. https://doi.org/10.1130/G23471A.1.

Flowers, R.M., 2009. Exploiting radiation damage control on apatite (U-Th)/He dates in cratonic regions. Earth Planet. Sci. Lett. 277, 148–155. https://doi.org/10.1016/j.epsl.2008.10.005.

Flowers, R.M., Ketcham, R.A., Shuster, D.L., Farley, K.A., 2009. Apatite (U-Th)/He thermochronometry using a radiation damage accumulation and annealing model. Geochim. Cosmochim. Acta 73, 2347–2365. https://doi.org/10.1016/j.gca.2009.01.015.

Flowers, R.M., Kelley, S.A., 2011. Interpreting data dispersion and " inverted" dates in apatite (U-Th)/He and fission-track datasets: An example from the US midcontinent. Geochim. Cosmochim. Acta 75, 5169–5186. https://doi.org/10.1016/j.gca.2011.06.016.

Gallagher, K., Stephenson, J., Brown, R., Holmes, C., Fitzgerald, P., 2005. Low temperature thermochronology and modeling strategies for multiple samples 1: Vertical profiles. Earth Planet. Sci. Lett. 237, 193–208. https://doi.org/10.1016/j.epsl.2005.06.025.

Gallagher, K., 2012. Transdimensional inverse thermal history modeling for quantitative thermochronology. J. Geophys. Res. Solid Earth, 117, 1–16. https://doi.org/10.1029/2011JB008825.

Galli, C.I., Coira, B., Alonso, R., Reynolds, J., Matteini, M., Hauser, N., 2014. Tectonic controls on the evolution of the Andean Cenozoic foreland basin: Evidence from fluvial system variations in the Payogastilla Group, in the Calchaquí, Tonco and Amblayo Valleys, NW Argentina. J. South Am. Earth Sci. 52, 234–259. https://doi.org/10.1016/j.jsames.2014.03.003.

Gautheron, C., Tassan-Got, L., Barbarand, J., Pagel, M., 2009. Effect of alpha-damage annealing on apatite (U-Th)/He thermochronology. Chem. Geol. 266, 157–170. https://doi.org/10.1016/j.chemgeo.2009.06.001.

Grier, M.E., Salfity, J.A., Allmendinger, R.W., 1991. Andean reactivation of the Cretaceous Salta rift, northwestern Argentina. Journal of South American Earth Sciences, 4(4), 351-372.

Gónzalez Villa, R., 2002. El Subgrupo Jujuy (Neógeno) entre los 24°-26° LS y 64°-66° LO, tramo centro-austral de la cadena subandina argentina, provincias de Salta y Jujuy. Unpublished PhD Thesis. Universidad Nacional de Salta, Argentina, pp. 136.

Hain, M.P., Strecker, M.R., Bookhagen, B., Alonso, R.N., Pingel, H., Schmitt, A.K., 2011. Neogene to Quaternary broken foreland formation and sedimentation dynamics in the Andes of NW Argentina (25°S). Tectonics 30, 1–27. https://doi.org/10.1029/2010TC002703.

Hernández, M., Franzese, J.R., Vergani, G.D., 2016. Caracterización Estructural del Anticlinal Tin Tin: Aspectos Sobre su Estilo de Deformación y su Relación con la Tectónica Cenozoica del Valle Calchaquí, Provincia de Salta. Rev. la Asoc. Geol. Argentina 73, 405–420.

Hilley, G.E., Strecker, M.R., 2004. Steady state erosion of critical Coulomb wedges with applications to Taiwan and the Himalaya. J. Geophys. Res. Solid Earth 109, 1–17. https://doi.org/10.1029/2002jb002284.

Hilley, G.E., Strecker, M.R., 2005. Processes of oscillatory basin filling and excavation in a tectonically active orogen: Quebrada del Toro Basin, NW Argentina. Bull. Geol. Soc. Am. 117, 887–901. https://doi.org/10.1130/B25602.1.

Holdsworth, R.E., Hand, M., Miller, J.A., Buick, I.S., 2001. Continental Reactivation and Reworking: an introduction. In: Miller, J.A., Holdsworth, R.E., Buick, I.S., Hand, M. (Eds.), Continental Reactivation and Reworking, pp. 1–12.

Hongn, F.D., Seggiaro, R.E., 2001. Hoja Geológica 2566-III, Cachi, 1:250.000. Provincias de Salta y Catamarca. In: Servicio Geológico Minero Argentino, Boletín 248, pp. 87. Buenos Aires.

Hongn, F., del Papa, C., Powell, J., Petrinovic, I., Mon, R., Deraco, V., 2007. Middle Eocene deformation and sedimentation in the Puna-Eastern Cordillera transition (23°-26°S): Control by preexisting heterogeneities on the pattern of initial Andean shortening. Geology, 35, 271–274. https://doi.org/10.1130/G23189A.1.

Hongn, F., Mon, R., Petrinovic, I. Del Papa, C., Powell, J. 2010. Inversión y reactivación tectónicas cretácico-cenozoicas en el noroeste argentino: influencia de las heterogeneidades del basamento neoproterozoico-paleozoico inferior. Revista de la Asociación Geológica Argentina; Lugar: Buenos Aires; 66, 38-53.

Hurford, A.J., Green, P.F., 1982. A user's guide to fission track dating calibration. Earth Planet. Sci. Lett. 59, 343–354. https://doi.org/10.1016/0012-821X(82)90136-4.

Hurford, A.J., Green, P.F., 1983. The zeta age calibration of fission-track dating. Isot. Geosci. 1, 285–317. https://doi.org/10.1016/S0009-2541(83)80026-6.

Jordan, T.E., Alonso, R.N., 1987. Cenozoic stratigraphy and Basin Tectonics of the Andes Mountain, 20-28 South Latitude. American Association of Petroleum Geologist, 71, 49-64. Tulsa.

Jordan, T.E., Isacks, B.L., Allmendinger, R.W., Brewer, J.A., Ramos, V.A., Ando, C.J., 1983. Andean tectonics related to geometry of the subducted Nazca plate. Geol. Soc. Am. Bull. 94, 341–361.

Ketcham, R.A., Donelick, R.A., Carlson, W.D., 1999. Variability of apatite fission-track annealing kinetics: III. Extrapolation to geological time scales. Am. Mineral. 84, 1235–1255. https://doi.org/10.2138/am-1999-0902.

Ketcham, R.A., Carter, A., Donelick, R.A., Barbarand, J., Hurford, A.J., 2007. Improved modeling of fission-track annealing in apatite. Am. Mineral. 92, 799–810. https://doi.org/10.2138/am.2007.2281.

Kley, J. and Monaldi, C.R., 2002. Tectonic inversion in the Santa Barbara System of the central Andean foreland thrustbelt, northwestern Argentina. Tectonics, 21(6): 1061, doi:10.1029/2002TC902003.

Kortyna, C., DeCelles, P.G., Carrapa, B., 2019. Structural and thermochronologic constraints on kinematics and timing of inversion of the Salta rift in the Tonco-Amblayo sector of the Andean retroarc fold-thrust belt, northwestern Argentina, Andean Tectonics. Elsevier Inc. https://doi.org/10.1016/b978-0-12-816009-1.00018-6.

Lenters, J., Cook, K.L., 1997. On the origin of the Bolivian high and related circulation features of the South American climate. J. Atmos. Sci.54, 656–678.

Lisker, F., Ventura, B., Glasmacher, U.A., 2009. Apatite thermochronology in modern geology. Geol. Soc. Spec. Publ. 324, 1–23. https://doi.org/10.1144/SP324.1.

Marquillas, R.A., del Papa, C.E., Sabino, I.F., 2005. Sedimentary aspects and paleoenvironmental evolution of a rift basin: Salta Group (Cretaceous – Paleogene), northwestern Argentina. International Journal of Earth Sciences, 94(1), 94-113. https://doi.org/10.1007/s00531-004-0443-2.

Masek, G., Duncan, C., 1998. Minimum-work mountain building. J. Geophys. Res. 103, 907–917.

McCarthy, J. A., Schoenbohm, L. M., Bierman, P. R., Rood, D., Hidy, A. J., 2019. Late Quaternary tectonics, incision, and landscape evolution of the Calchaquí River Catchment, Eastern Cordillera, NW Argentina. Journal of Geophysical Research: Earth Surface,124. https://doi.org/10.1029/2019JF005091.

Montero Lopez, C., Aramayo, A., Ballato, P., 2017. New evidences of the Paleogene and Early Miocene unconformity in the Quebrada de Carachi, El Toro basin, Cordillera Oriental (NW Argentina), in: XX Congreso Geológico Argentino. San Miguel de Tucumán, Argentina.

Mulch, A., Uba, C.E., Strecker, M.R., Schoenberg, R., Chamberlain, C.P., 2010. Late Miocene climate variability and surface elevation in the central Andes. Earth Planet. Sci. Lett. 290, 173–182. https://doi.org/10.1016/j.epsl.2009.12.019.

Murray, K.E., Braun, J., Reiners, P.W., 2018. Toward Robust Interpretation of Low-Temperature Thermochronometers in Magmatic Terranes. Geochemistry, Geophysics, Geosystems, 19, 3739–3763. https://doi.org/10.1029/2018GC007595.

Noe, Y.E., Gonzalez, A.C., Elena, H.J., Bianchi, A.R., 2012. Mapa de isohietas anuales del Noroeste Argentino. Instituto Nacional de Tecnología Agropecuaria.

Payrola Bosio, P.A., Powell, J., Papa, C. del, Hongn, F., 2009. Middle Eocene deformation-sedimentation in the Luracatao Valley: Tracking the beginning of the foreland basin of northwestern Argentina. J. South Am. Earth Sci. 28, 142–154. https://doi.org/10.1016/j.jsames.2009.06.002.

Payrola, P.A., Hongn, F., Cristallini, E., García, V., del Papa, C., 2012. Andean oblique folds in the Cordillera Oriental - Northwestern Argentina: Insights from analogue models. J. Struct. Geol. 42, 194–211. https://doi.org/10.1016/j.jsg.2012.05.003.

Payrola, P.A., del Papa, C., Aramayo, A., Pingel, H., Hongn, F., Sobel, E.R., Zeilinger, G., Strecker, M.R., Zapata, S., Cottle, J., Salado Paz, N., Glodny, J., 2020. Episodic out-of-sequence deformation promoted by Cenozoic fault reactivation in NW Argentina. Tectonophysics 776, 228276. https://doi.org/10.1016/j.tecto.2019.228276.

Pearson, D.M., Kapp, P., Reiners, P.W., Gehrels, G.E., Ducea, M.N., Pullen, A., Otamendi, J.E., Alonso, R.N., 2012. Major Miocene exhumation by fault-propagation folding within a metamorphosed, early Paleozoic thrust belt: Northwestern Argentina. Tectonics 31. https://doi.org/10.1029/2011TC003043.

Pearson, D.M., Kapp, P., DeCelles, P.G., Reiners, P.W., Gehrels, G.E., Ducea, M.N., Pullen, A., 2013. Influence of pre-Andean crustal structure on Cenozoic thrust belt kinematics and shortening magnitude: Northwestern Argentina. Geosphere 9, 1766–1782. https://doi.org/10.1130/GES00923.1.

Pingel, H., Strecker, M.R., Alonso, R.N., Schmitt, A.K., 2013. Neotectonic basin and landscape evolution in the Eastern Cordillera of NW Argentina, Humahuaca Basin (~24ºS). Basin Res. 25, 554e573.

Pingel, H., Alonso, R. N., Mulch, A., Rohrmann, A., Sudo, M., & Strecker, M. R., 2014. Pliocene orographic barrier uplift in the southern Central Andes. Geology, 42(8), 691–694. https://doi.org/10.1130/G35538.1.

Pingel, H., Mulch, A., Alonso, R.N., Cottle, J., Hynek, S.A., Poletti, J., Rohrmann, A., Schmitt, A.K., Stockli, D.F., Strecker, M.R., 2016. Surface uplift and convective rainfall along the southern Central Andes. Earth Planet. Sci. Lett. 440, 33–42. https://doi.org/10.1016/j.epsl.2016.02.009.

Pingel, H., Schildgen, T., Strecker, M. R., & Wittmann, H., 2019. Pliocene–Pleistocene orographic control on denudation in northwest Argentina. Geology, 47(4), 359–362. https://doi.org/10.1130/G45800.1.

Pingel, H., Strecker, M. R., Mulch, A., Alonso, R. N., Cottle, J., & Rohrmann, A., 2020. Late Cenozoic topographic evolution of the Eastern Cordillera and Puna Plateau margin in the southern Central Andes (NW Argentina). Earth and Planetary Science Letters, 535, 116112. https://doi.org/10.1016/j.epsl.2020.116112.

Reiners, P.W., Thomson, S.N., Vernon, A., Willett, S.D., Zattin, M., Einhorn, J., Gehrels, G., Quade, J., Pearson, D., Murray, K.E., Cavazza, W., 2015. Low-temperature thermochronologic trends across the central Andes, 21°S-28°S. Mem. Geol. Soc. Am. 212, 215–249. https://doi.org/10.1130/2015.1212(12).

Riller, U., Hongn, F., 2003. Structural influence of Paleozoic discontinuities on Cretaceous to Quaternary tectonism in the Eastern Cordillera, NW-Argentina. Eur. Geophys. Soc. (Contributions EGS.AGU-EUG Joint Assembly, Nice, April 2003), Geophysical Research Abstracts, 5, 02303.

Rohrmann, A., Sachse, D., Mulch, A., Pingel, H., Tofelde, S., Alonso, R.N., Strecker, M.R., 2016. Miocene orographic uplift forces rapid hydrological change in the southern central Andes. Sci. Rep. 6, 1–7. https://doi.org/10.1038/srep35678.

Salfity, J.A., 2004. Geología Regional Del Valle Calchaquí, Argentina. An. la Acad. Ciencias Exactas Físicas y Nat. Bs. As. 56, 133–150.

Salfity, J.A. y C.R. Monaldi, 2006. Hoja Geológica 2566-IV, Metán, escala 1:250.000. Instituto de Recursos Minerales. Servicio Geológico Minero Argentino, Boletín 319, 74 pp. Buenos Aires.

Sibson, R.H., 1995. Selective fault reactivation during basin inversion: potential for fluid redistribution through fault-valve action. In: Buchanan, J.G., Buchanan, P.G. (Eds.), Bain Inversion. 88. Geological Society of London, Special Publications, pp. 3–19.

Sobel, E.R., Strecker, M.R., 2003. Uplift, exhumation and precipitation: Tectonic and climatic control of Late Cenozoic landscape evolution in the northern Sierras Pampeanas, Argentina. Basin Res. 15, 431–451. https://doi.org/10.1046/j.1365-2117.2003.00214.x.

Strecker, M.R., Alonso, R.N., Bookhagen, B., Carrapa, B., Hilley, G.E., Sobel, E.R., Trauth, M.H., 2007. Tectonics and Climate of the Southern Central Andes. Annu. Rev. Earth Planet. Sci. 35, 747–787. https://doi.org/10.1146/annurev.earth.35.031306.140158.

Turner, J.C.M., 1959. Estratigrafía del cordón de Escaya y de la sierra Rinconada. Revista de la Asociación Geológica Argentina, 15, 15-39.

Turner, J.C.M., 1960. Estratigrafía de la Sierra de Santa Victoria y adyacencias. Boletín de la Academia Nacional de Ciencias de Córdoba 41, 163-196.

Turner, J.C.M., 1979. Geología Regional Argentina. Academia Nacional de Ciencias, Córdoba (1691 pp).

Vera, C., Baez, J., Douglas, M., Emmanuel, C.B., Marengo, J., Meitin, J., Nicolini, M., Nogues-Paegle, J., Peagle, J., Penalba, O., Salio, P., Saulo, C., Silva Dias, M.A., Silva Dias, P., Zipser, E., 2006. The South American Low-Level Jet Experiment. Bull. Am. Meteorol. Soc. 63–78.

Vergani, G., Starck, D., 1989. Aspectos Estructurales del Valle de Lerma, al Sur de la Ciudad de Salta. Boletín Inf. Pet.

Wagner, G.A., Gleadow, A.J.W., Fitzgerald, P.G., 1989. The significance of the partial annealing zone in apatite fission-track analysis: Projected track length measurements and uplift chronology of the transantarctic mountains. Chem. Geol. Isot. Geosci. Sect. 79, 295–305. https://doi.org/10.1016/0168-9622(89)90035-3.

Wagner, G.A., Van den Haute, P., 1992. Fading of Fission Tracks, in: Fission-Track Dating. Solid Earth Sciences Library, Vol 6. Springer, Dordrecht. pp. 95–119. https://doi.org/10.1007/978-94-011-2478-2_4.

Willett, S.D., 1999. Orogeny and orography: The effects of erosion on the structure of mountain belts. J. Geophys. Res. Solid Earth 104, 28957–28981. https://doi.org/10.1029/1999jb900248.

Wolf, R.A., Farley K.A. and Kass D.M., 1998. Modeling of the temperature sensitivity of the apatite (U–Th)/He thermochro- nometer. Chem. Geol. 148, 105–114.

Yagupsky, D.L., Brooks, B.A., Whipple, K.X., Duncan, C.C., Bevis, M., 2014. Distribution of active faulting along orogenic wedges: Minimum-work models and natural analogue. J. Struct. Geol. 66, 237–247. https://doi.org/10.1016/j.jsg.2014.05.025.

Zapata, S., Sobel, E.R., del Papa, C., Muruaga, C., Zhou, R., 2019a. Miocene fragmentation of the Central Andean foreland basins between 26 and 28°S. J. South Am. Earth Sci. 94, 18. https://doi.org/10.1016/j.jsames.2019.102238.

Zapata, S., Sobel, E.R., del Papa, C.E., Jelinek, A.R., Glodny, J., 2019b. Using a Paleosurface to Constrain Low-Temperature Thermochronological Data Tectonic Evolution of the Cuevas Range, Central Andes. Tectonics 38, 3939–3958. https://doi.org/https://doi.org/10.1029/2019TC005887.

Zapata, S., Sobel, E. R., Del Papa, C., Glodny, J., 2020. Upper plate controls on the formation of broken foreland basins in the Andean retroarc between 26°S and 28°S: From Cretaceous rifting to Paleogene and Miocene broken foreland basins. Geochemistry, Geophysics, Geosystems, 21, e2019GC008876. https://doi.org/10.1029/2019GC008876

Zeitler, P.K., Herczeg, A.L., McDougall, I., Honda, M., 1987. U-Th-He dating of apatite: A potential thermochronometer. Geochim. Cosmochim. Acta 51, 2865–2868. https://doi.org/10.1016/0016-7037(87)90164-5.

Zhou, R., Schoenbohm, L.M., Sobel, E.R., Davis, D.W., Glodny, J., 2017. New constraints on orogenic models of the southern Central Andean Plateau: Cenozoic basin evolution and bedrock exhumation. Bull. Geol. Soc. Am. 129, 152–170. https://doi.org/10.1130/B31384.1.

Sample	H (m)	Lat (º S)	Long. (º W)	Stratigraphic unit	age (Ma)		Raw (Ma)	(Ma)	(Ma)	U (ppm)	(ppm)	(ppm)	eU	He (nmol/g)	Ft	ESR (μm)	Term.
PC1	5100	25.074583	5.852036	Puncoviscana	600-530	PC1-a	6.4	10.2	0.4	60	68	19	76	2.62	0.63	40	1
				Fm		PC1-b	3.5	5.1	0.5	9	22	32	14	0.27	0.68	47	2
						PC1-c	4.1	6.8	0.4	27	65	12	42	0.95	0.61	38	1
						PC1-d	4.2	6.5	0.3	29	34	41	37	0.84	0.64	42	1
						PC1-e	4.3	7.1	0.3	53	58	114	67	1.58	0.61	39	1
PC1.1	4900	25.071743	65.85688	Puncoviscana	600-530	PC1.1a	6.6	10.1	0.4	66	76	53	84	3.01	0.66	44	1
				Fm		PC1.1b	5.0	8.1	0.5	29	19	60	34	0.91	0.61	39	1
						PC1.1c	4.2	6.5	2.3	2	17	8	6	0.13	0.64	41	1
						PC1.1d	4.9	7.4	0.3	63	89	55	84	2.26	0.67	45	0
PC1.2	4740	25.071947	65.85936	Puncoviscana	600-530	PC1.2a	3.8	6.2	1.5	7	3	36	8	0.17	0.62	39	1
				Fm													
PC2	4551	25.074162	65.86396	Puncoviscana	600-530	PC2-a	4.2	5.9	0.3	27	18	45	31	0.72	0.71	52	1
				Fm		PC2-b	4.1	4.6	0.1	7	2	1	7	0.16	0.88	122	1
						PC2-c	3.4	4.5	0.2	19	5	10	20	0.36	0.76	62	0
						PC2-e	3.7	5.3	2.8	1	6	1	2	0.04	0.70	49	1
PC2.1	4405	25.071146	65.86561	Puncoviscana	600-530	PC2.1a	3.9	6.1	0.4	41	124	25	70	1.47	0.63	41	0
				Fm													
PC3	4257	25.070608	65.86945	Puncoviscana	600-530	PC3-a	3.3	5.4	1.6	6	7	2	7	0.13	0.62	39	1
				Fm		PC3-b	5.0	7.0	0.1	30	146	14	65	1.78	0.73	55	1
						PC3-c	2.9	4.2	0.4	18	36	4	27	0.41	0.68	47	0
						PC3-e		3.6	2.6	4	10	4	7	0.07	0.57	35	0
PC3.1	4045	25.075715	65.87382	Puncoviscana	600-530	PC3.1a	7.0	9.2	0.5	3	13	6	6	0.24	0.76	62	0
				Fm		PC3.1b	4.1	6.1	0.1	134	166	29	173	3.80	0.67	45	0
						PC3.1c	3.9	6.4	0.4	36	95	65	59	1.26	0.61	39	0
						PC3.1d	3.9	6.6	1.0	19	9	32	21	0.46	0.59	37	0

Table 1 AHe data

Sample	H (m)	Lat (° S)	Long (° W)	n	*Rho*D		Mean (μm)	(μm)					(Ma)	(Ma)	(%)
PC1.1	**4900**	**25.071743**	**65.85688**	**18**	**8.1**	**5000**	**1.79**	**0.24**	**1.76**	**102**	**5.34**	**310**	**133 (P1)**	**37.3**	**44**
				7			**1.81**	**0.23**					**15.8 (P2)**	**5.1**	**72**
PC1.2	**4740**	**25.071947**	**65.85936**	**35**	**7.2**	**5000**	**2.27**	**0.82**	**0.97**	**136**	**10.37**	**1460**	**11.5**	**1.4**	**49**
PC2	**4551**	**25.074162**	**65.86396**	**19**	**7.3**	**5000**	**2.09**	**0.35**	**1.01**	**56**	**13.55**	**749**	**9.4**	**1.5**	**88**
PC2.1	**4405**	**25.071146**	**65.86561**	**27**	**7.4**	**5000**	**1.83**	**0.25**	**0.89**	**78**	**11.43**	**998**	**10.5**	**1.6**	**11**
PC3.1	**4045**	**25.075715**	**65.87382**	**37**	**8.2**	**5000**	**1.91**	**0.53**	**0.69**	**100**	**12.02**	**1724**	**8.20**	**1.00**	**21**

Table 2: AFT data

Exhumation and structural evolution of the high-elevation Malcante Range, Eastern Cordillera, NW Argentina

Highlights

Calchaquí high-mountains with anomalous position.

Angular unconformity in the contact between Paleogene post-rift deposits and middle Eocene foreland deposits.

Malcante Range exhumation start at 10 Ma.

Accelerated uplifting during the Pliocene.

Declaration of interests

☒ The authors declare that they have no known competing financial interests or personal relationships that could have appeared to influence the work reported in this paper.

☐The authors declare the following financial interests/personal relationships which may be considered as potential competing interests: